2013

High Resolution Tephra and U/Pb Chronology of the 3.33 – 3.26 Ga Mendon Formation, Barberton, Greenstone Belt, South Africa

Nicholas Burns Decker
Louisiana State University and Agricultural and Mechanical College, anewfad@gmail.com

HIGH RESOLUTION TEPHRA AND U/PB CHRONOLOGY OF THE 3.33 – 3.26 GA MENDON FORMATION, BARBERTON GREENSTONE BELT, SOUTH AFRICA

A Thesis

Submitted to the Graduate Faculty of the
Louisiana State University and
Agricultural and Mechanical College
In partial fulfillment of the
requirements for the degree of
Master of Science

in

The Department of Geology and Geophysics

by
Nicholas Burns Decker
B.S., Louisiana State University, 2010
May 2013

Acknowledgements

The author is especially grateful to Dr. Gary Byerly, his advisor, for his ever insightful guidance, an excellent field season, and a worthwhile project. He would also like to thank Dr. Byerly, Dr. Don Lowe and his student Lizzy Stefurak, and Dr. Melanie Thompson-Stiegler for their contributions to his research for which they will be coauthors on when this manuscript is submitted for publication to Precambrian Research. The author would like to acknowledge Dr. Samuel Bentley for allowing him use of his handheld XRF system and to Dr. Bentley's students, Ashley Howell, Jill Bambrick Banks, and Kathryn Denommee for their help operating it. The author is also eternally grateful to Rick Young for helping process samples and repair lab equipment. Finally, the author would like to thank the staff of the WSU GeoAnalytical Lab and the Stanford SUMAC facility for their help acquiring and processing geochemical data.

Table of Contents

Abstract

The Mendon Formation in the Barberton Greenstone Belt of South Africa marks the boundary between the Onverwacht and Fig Tree Groups. These groups are characterized by mafic to ultramafic volcanism and felsic volcanism with related epiclastic sedimentation, respectively. This transition marks the end of komatiitic volcanism in the Barberton Greenstone Belt and is accompanied by numerous impact-related spherule layers. This study characterizes the upper Mendon Formation texturally and geochemically over a wide areal extent and across structure and facies change in an attempt to better understand the evolution of tectonic processes at this boundary. A suite of whole rock and handheld X-Ray Fluorescence analyses are presented in conjunction with textural information, stratigraphic relationships, and U/Pb ages to create a temporal and chemostratigraphic framework for the Mendon Formation. Local and regional stratigraphic variations, including absence of distinctive layers and variation in layer thickness, seen across the Mendon preclude ascription of a single stratigraphy that accurately describes the >1.2 km of section present in this formation. These variations indicate diachronous deposition of the Mendon over a wide areal extent and into multiple basins or sub-basins by more than one magmatic source. ^{204}Pb-corrected ^{206}Pb/^{238}U and ^{207}Pb/^{235}U concordia model ages of 3279 ± 9.1 Ma and 3287.3 ± 2.9 Ma for two samples from upper portions of the Mendon provide temporal context for deposition during the Mendon Formation. Two samples from the basal 10 m of the Fig Tree Group, above the S2 spherule bed that marks the boundary between the Onverwacht and Fig Tree Groups, give model ages of 3267.8 ± 6.9 Ma and 3261 ± 18 Ma. These ages provide added constraints for the Onverwacht-Fig Tree boundary and confirm that the Weltevreden Formation is roughly age-correlative with the uppermost Mendon Formation. While these formations are in part age-correlative and have similar lithologies, they do not appear to be

genetically related. The dominance of ultramafic volcanic rocks and the paucity of felsic volcanic and terrigenous sedimentary rocks within the Mendon and Weltevreden Formations indicate that the primary mode of crustal formation was likely plume-related magmatic accretion and not subduction. The relatively sharp transition within the BGB from ultramafic volcanic sequences to more felsic volcanic and epiclastic sedimentary sequences is everywhere marked by impact-related spherule layers, which suggest that major impacts may have played a role in the evolution of early Earth tectonics to more modern, subduction-related styles.

1. Introduction

Greenstone belts are somewhat enigmatic Archean crustal sequences that represent a large portion of preserved early crust and are typically composed of a variety of volcanic and sedimentary rocks that can be considered relatively unique to this early stage of Earth's evolution. There is still considerable debate over the tectonic processes and surface environments that gave rise to these terranes (de Wit et al., 2011; Furnes et al., 2013; Grove and Parman, 2004; Lowe and Byerly, 2007; Shirey and Richardson, 2011; Van Kranendonk, 2011a). One of the best preserved of these crustal sequences is the Barberton Greenstone Belt (BGB) of South Africa. Within this relatively well-studied supracrustal sequence, three stratigraphic groups appear to represent profoundly different tectonic settings: the Onverwacht Group, predominantly mafic to ultramafic lavas deposited on shallow marine platforms and likely the products of mantle plumes; the conformably overlying Fig Tree Group, predominantly felsic volcaniclastic detritus likely the products of subduction; and the Moodies Group, predominantly mature sands likely the products of plate collision, uplift and deep erosion of plutonic and high grade metamorphic rocks (Lowe and Byerly, 1999, 2007).

The Mendon Formation is a dominantly ultramafic volcanic succession that represents one of the last episodes of komatiitic volcanism in the BGB (Fig. 1), and its end gives rise to the beginning of widespread felsic volcanism and epiclastic sedimentation at the boundary between the Onverwacht and Fig Tree Groups (Lowe and Byerly, 1999, 2007). Understanding this sharp change in lithologies is essential to our understanding of what tectonic processes may have been occurring on the early Earth and how they evolved into more modern, subduction-related processes. Numerous impact-related layers have been identified in the BGB (Byerly et al., 2002; Kyte et al., 2003; Lowe and Byerly, 1986; Lowe et al., 1989; Lowe et al., 2003), many of which

occur at or near the Onverwacht-Fig Tree boundary. The relationship of these impact-related layers to this transition warrants closer investigation. Unfortunately, the stratigraphy of the Mendon is obscured by the complex structural deformation affecting the BGB (Lowe et al., 1999; Lowe et al., 2012), as well as systematic facies change observed across Mendon outcrops. Although a number of studies have characterized the lavas and ashes of this formation texturally and chemically (Byerly, 1999; Byerly et al., 1996; Lowe, 1999b, c; Thompson-Stiegler et al., 2008, 2010, 2011), the Mendon remains one of the least studied and most poorly understood formations in the BGB.

The aim of this study is to better describe the stratigraphy of the Mendon Formation, particularly the relatively poorly constrained upper Mendon, and improve our understanding of the tectonic evolution of the BGB during this time. Utilizing geochemical and textural analyses, samples collected from previously unstudied Mendon outcrops across the belt are described in order to place them in a temporal and spatial stratigraphic context. The temporal component of this stratigraphy is constrained by single zircon geochronology and by tracing chemically and texturally distinct units across structure and facies change. Interpretation of this stratigraphy provides a window into the relationships between the komatiitic flow rocks and associated tuffs, the evolution of the tectonic processes occurring during the formation of these rocks, and the potential instigators for the transition in tectonic styles recorded in the Onverwacht-Fig Tree boundary.

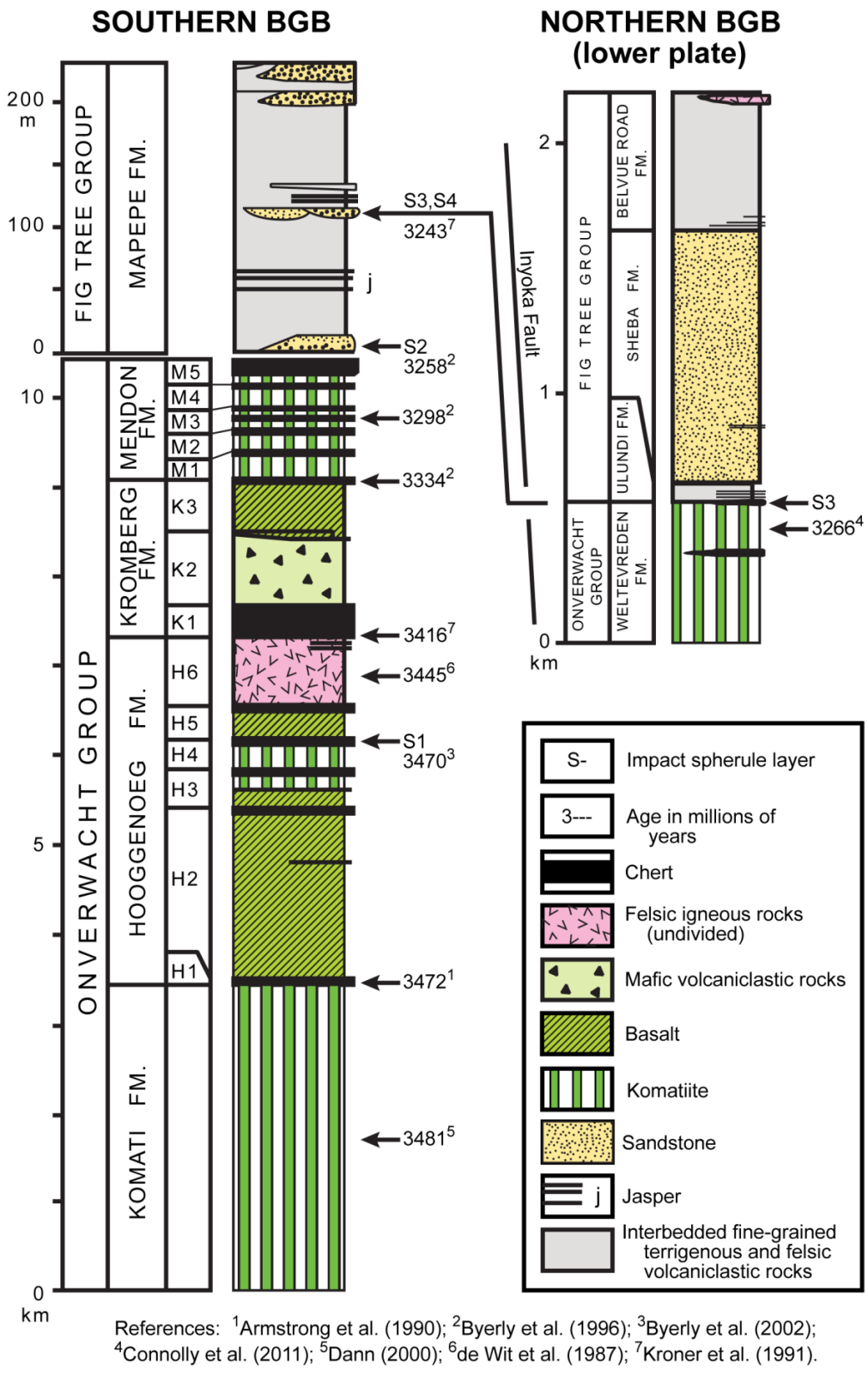

Figure 1. Generalized stratigraphic column of the BGB (Modified from Lowe et al., 2003; Thompson-Stiegler et al., 2011).

2. Geologic Setting

2.1. Barberton Greenstone Belt

The BGB is a mid-Archean supracrustal sequence composed of volcanic and sedimentary rocks that are among the oldest, most well-exposed, and best-preserved rocks on Earth. From base to top, this sequence is divided into three major lithostratigraphic units: the Onverwacht, Fig Tree (Fig. 1), and Moodies groups (Lowe and Byerly, 1999, 2007). The Onverwacht Group consists primarily of mafic and ultramafic volcanic rocks with interbedded volcaniclastics and cherts. The Fig Tree Group is a dominantly sedimentary and felsic volcanic sequence. The stratigraphic sequence is capped by the Moodies Group, which is a sedimentary sequence composed primarily of mature, quartz-rich sandstones.

The 8-10 km thick Onverwacht Group is subdivided into a total of seven formations (Lowe and Byerly, 1999, 2007). The Inyoka Fault divides the Onverwacht into distinct northern and southern domains (Fig. 2). Six of the formations, the Sandspruit, Theespruit, Komati, Hoogenoeg, Kromberg, and Mendon, are only found in the domain south of the Inyoka Fault. The seventh and final formation, the Weltevreden, is the only formation in the Onverwacht found north of the Inyoka Fault and is thought to be age-correlative with upper cycles of the Mendon Formation (Byerly et al., 1996; Lowe and Byerly, 1999). Both formations are characterized by effusive and pyroclastic komatiitic volcanism, but their overall stratigraphy, unit thicknesses, and modes of alteration are different.

2.2. Mendon Formation

The Mendon Formation, upon which this study focuses, is sequence of komatiitic volcanics interbedded with 1 to 35 m thick cherts (Byerly, 1999; Lowe and Byerly, 1999). The

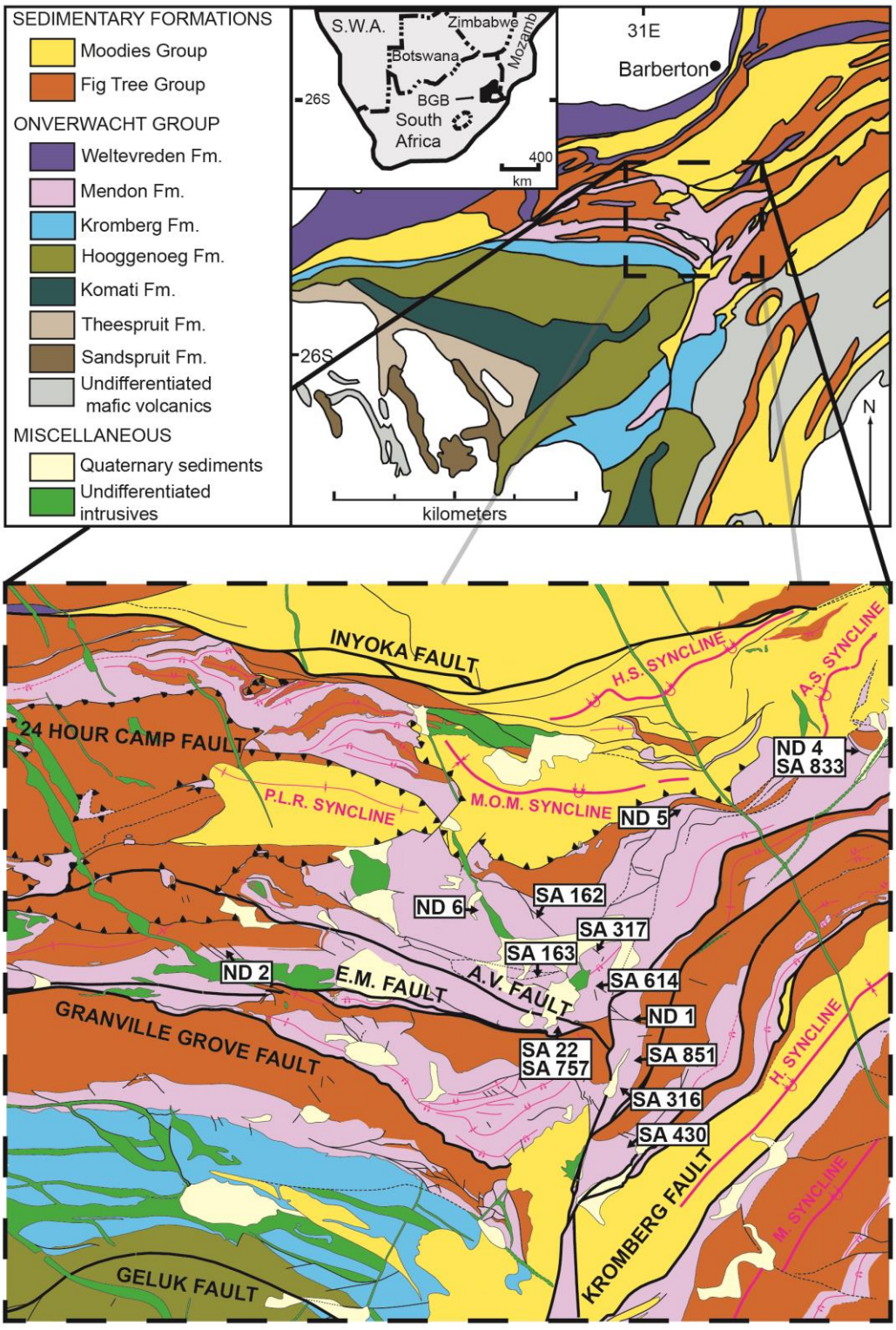

Figure 2. Generalized geologic map of the BGB. Enlarged section is a more detailed geologic map showing sample locations, structural features, and formation relationships (Modified from Lowe et al. 2012).

maximum aggregate thickness of the formation exceeds 1000 m, but assigning a representative thickness is challenging due to facies change and faulting (Figs. 2 and 3). This sequence is somewhat cyclic and has been described in terms of at least three major cycles: M1, M2, and M3. These cycles are further subdivided into volcanic and cherty sequences (i.e. M1v and M1c). The lowest of the cycles, M1, is a single 200-250 m thick, massive komatiite (M1v) overlain by the Msauli Chert (M1c), a distinctive, 20-35 m thick sequence of volcaniclastics and interbedded carbonaceous cherts that is present in most exposures of the Mendon Formation. In localities south of the Granville Grove Fault, M1c is succeeded by 20-50 m of banded ferruginous cherts and the basal rocks of the Fig Tree. In sections to the north of this fault, M1c is overlain by 100-150 m of komatiites (M2v) and 2-10 m of komatiitic ash, accretionary lapilli, and lapilli tuff (M2c). This is sometimes followed by 40 m of komatiites and komatiitic basalts (M3v) and 1-2 m of komatiitic ash, accretionary lapilli, and black chert (M3c). Higher Mendon cycles, up to and possibly surpassing M5, have been identified and have been previously found to lack volcaniclastic portions (Thompson-Stiegler et al., 2010). There is a general younging trend observed in rocks moving from southwest to northeast as structure and facies change are encountered (Fig. 3). These changes have been interpreted as the result of active rifting occurring at the time of Mendon deposition (Byerly, 1999; Lowe, 1999a; Lowe and Byerly, 2007), and that more northeastern sections were deposited into ever-deepening basins. This accounts for the increasing number of upper Mendon cycles that accompanies the observed younging trend. Stratigraphy in the Mendon is further complicated by the lack of a complete section. Sections containing the lowest Mendon cycles tend not to contain upper cycles, likely due to this syndepositional rifting.

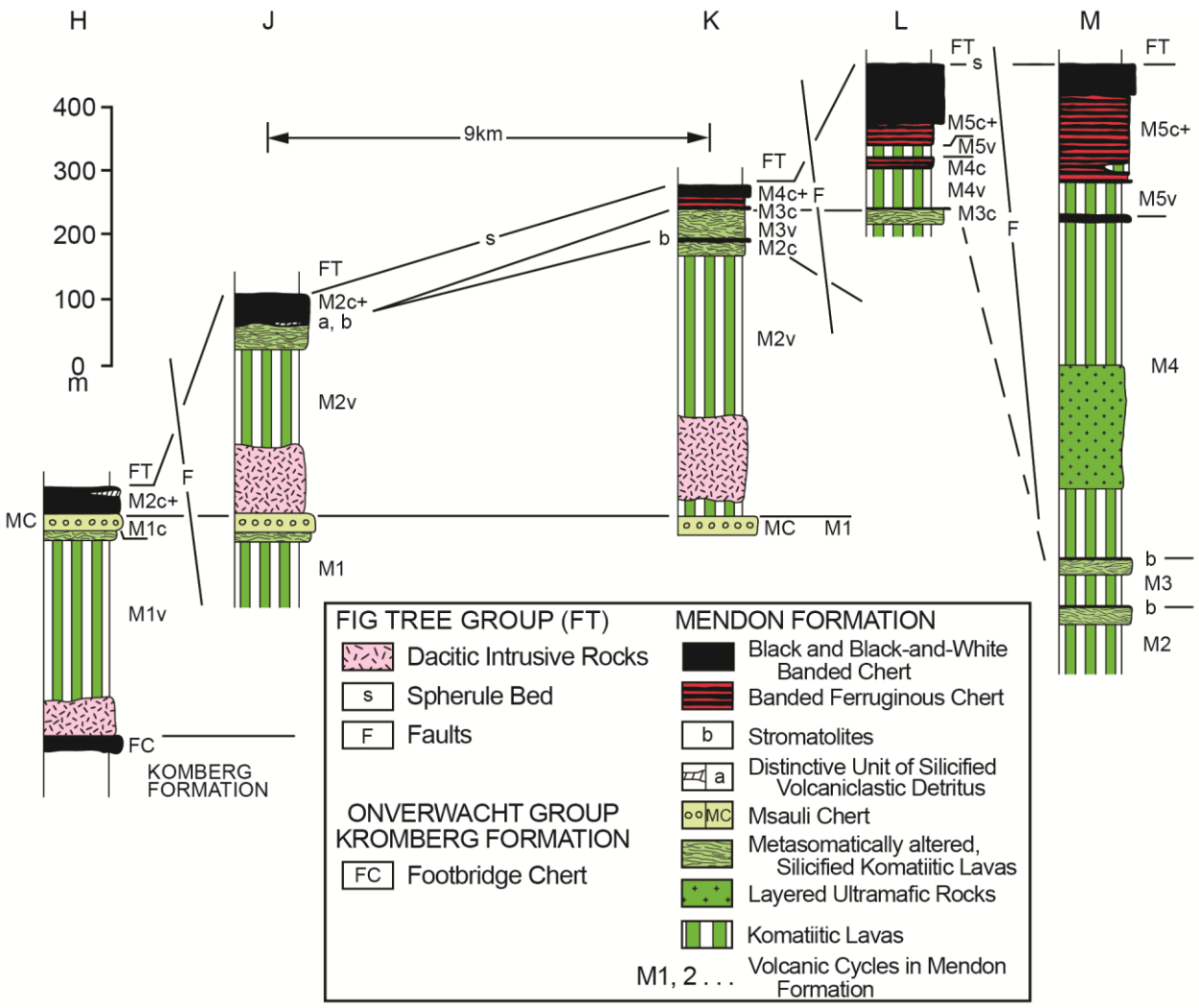

Figure 3. Fence diagram illustrating stratigraphic and lithologic variations in five locations across structure and facies change (Redrafted from Lowe and Byerly, 1999; locations of sections shown in Fig. 5 of that paper).

The volcaniclastic materials in these cycles are predominantly silicified ultramafic (komatiitic basalt to komatiite in composition) tuffs with abundant accretionary lapilli. These accretionary lapilli exhibit preservation of fine internal structuring (Lowe, 1999c). They are distinctive with respect to individual cycles and can be distinguished based on textural features and chemical composition (Fig. 4) (Thompson-Stiegler et al., 2008, 2010). Mendon komatiites are also distinctive and can be distinguished geochemically based on both whole-rock and

chrome spinel analyses (Byerly, 1999). The majority of Mendon tuffs and the tops of lava flows have been subjected to extensive, early-stage silicification (Byerly, 1999; Hofmann and Harris, 2008; Lowe, 1999c). A few mechanisms have been proposed to explain this alteration, such as excess silica due to the lack of silica-secreting organisms that exist today (Siever, 1992) leading to interactions with Si-saturated seawater at the sediment-water interface (Hofmann, 2005; Hofmann and Harris, 2008; Lowe, 1999b) or circulation of hydrothermal fluids (Duchac and Hanor, 1987; Hanor and Duchac, 1990). Silicification has provided for preservation of primary textures and prevented much compaction, which is particularly evident in accretionary lapilli beds. Unfortunately, this has also resulted in alteration of primary compositions via replacement with Si and K as well as REE mobilization. Bulk ash compositions are typically dominated by Al_2O_3, SiO_2, and K_2O. Bulk chemical analyses can be misleading, and geochemical studies must instead focus on immobile element (Al, Ti, P, Cr, Y, V, Zr) ratios, such as Ti/Zr, Cr/Zr, and Al_2O_3/TiO_2 (Hofmann and Harris, 2008; Rouchon and Orberger, 2008). While these "immobile" elements may have been mobilized in various portions of a flow or sedimentary unit, their ratios are constant throughout (Thompson-Stiegler et al., 2010). This allows samples from any portion of a unit to be successfully correlated to the same unit elsewhere.

Age constraints for the base of the Mendon Formation have been given by a 3334 ± 3 Ma, 5 cm thick felsic tuff in the 15-25 m sequence of black and black-and-white banded cherts known as the Footbridge Chert, which defines the top of the underlying Kromberg Formation (Byerly et al., 1996). As the Mendon Formation and Fig Tree Group chronologically interfinger at different localities across the BGB, age constraints for the top of the Mendon Formation are given by multiple dates. The base of the overlying Fig Tree Group has been dated at 3259 ± 4

Ma (Kröner et al., 1991) and multiple felsic tuffs in M3c have given a mean age of 3298 ± 3 Ma (Byerly et al., 1996).

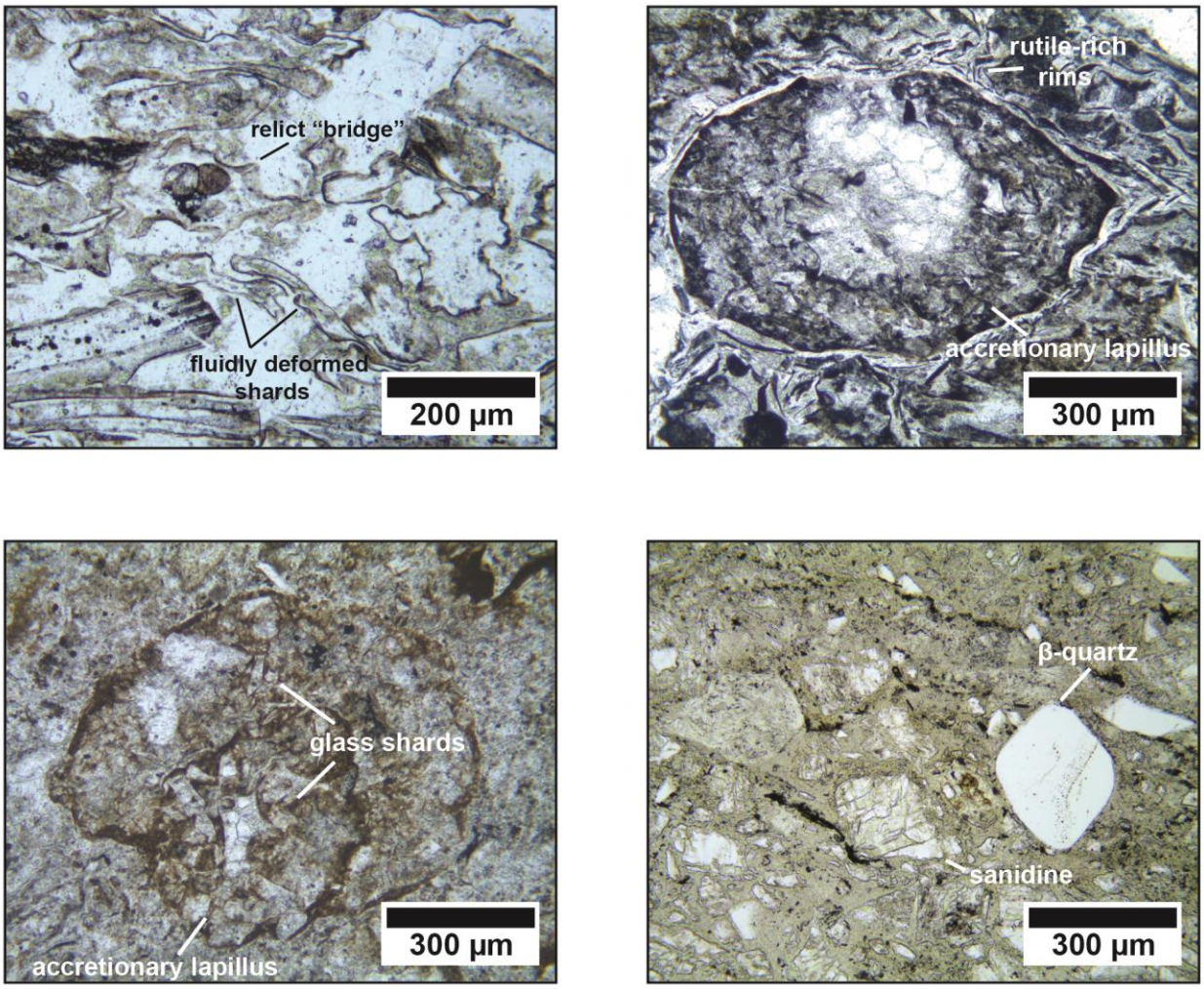

Figure 4. Photomicrographs of Mendon and Fig Tree tuffs. (top left) Felsic ash from M3c2; sample ND 2-7. Glass shards in this ash display stretched vesicles and relict "bridges" where shards were connected and broke apart during cooling. (top right) Distinctive accretionary lapillus from M3c; sample ND 5-4B. Lenticular fibers are rutile-rich rims that peeled off of pyroclasts pre-silification. (bottom left) Accretionary lapillus typical of M3c; sample ND 4-4. (bottom right) Dacitic tuff from the basal 10 m of the Fig Tree; sample SA 915-1. Tuff is crystal rich and contains abundant sanidine and β-quartz.

2.3. Komatiites and Pyroclastic Komatiitic Volcanism

Komatiites are highly-magnesian, ultramafic extrusive rocks that were, with one exception (Arndt et al., 1997; Echeverria, 1980), only erupted in the Precambrian. They contain > 18 wt.% MgO (Le Bas, 2000) and typically exhibit olivine or pyroxene spinifex textures, a distinctive textural feature unique to the upper chilled margins of komatiitic flows (Nesbitt et al., 1982). Considering that they make up a large portion of preserved crust in the BGB and are relics of magmatic processes that are no longer functioning on Earth, these enigmatic rocks are an important key to our understanding of active processes during this time and the evolution of tectonics throughout Earth history. Studies have interpreted komatiites as the result of anhydrous partial melting in mantle plumes (Arndt, 2003; Arndt et al., 1997; Byerly, 1999; Campbell et al., 1989; Hanski et al., 2001; Sproule et al., 2002; Thompson-Stiegler et al., 2010) or hydrous partial melting in a subduction-related setting (de Wit, 1998; de Wit et al., 2011; Furnes et al., 2013; Furnes et al., 2011; Grove and Parman, 2004; Parman et al., 2004). The relative paucity of more felsic, arc-related volcanics in much of the BGB argues for a plume genesis and suggests basaltic-to-komatiitic volcanism may represent the dominant method of crustal formation in the early-to-mid-Archean. Komatiites are typically classified based on their Al_2O_3/TiO_2 ratios, which are related to the depth of melting for their source magmas (Jahn et al., 1982). The three major subtypes are Al-depleted komatiites ($Al_2O_3/TiO_2 < 15$), Al-undepleted komatiites ($15 < Al_2O_3/TiO_2 < 30$), and Al-enriched komatiites ($Al_2O_3/TiO_2 > 30$). However, these subtypes are broad and also cover the variation of TiO_2. It is necessary to keep the composition of both Al_2O_3 and TiO_2 in mind when interpreting these ratios.

Pyroclastic volcanism involving komatiitic lavas was initially thought unlikely due to the low viscosity and low volatile content of komatiitic magmas. Recent studies (Ransom et al.,

1999; Thompson-Stiegler et al., 2008, 2011) have shown that it is possible for komatiitic eruptions to be explosive and that tuffs of pyroclastic komatiitic fallout may comprise up to 95% of the material in some cherts interbedded between lava flows in the Onverwacht. Eruptions were probably phreatomagmatic based on the lack of volatiles in the magmas and the juvenile nature of pyroclasts. The mechanism for these eruptions was likely molten fuel-coolant interactions (MFCI). Optimal water-magma ratios of 0.03 to 0.04 are required to produce the uniformly fine grain size seen in these tuffs, and eruptions were necessarily shallow for the eruption column to be able to escape the water column (Thompson-Stiegler et al., 2011). These depth constraints indicate that flows built up in marine basins until an eruption occurred at shallow depths, <10 m, that resulted in phreatomagmatic activity and an eruption column that deposited komatiitic ash tens-to-hundreds of kilometers away from the vent.

3. Methods

3.1. Bulk Rock X-Ray Fluorescence

Twenty-two samples were selected to be sent to Washington State University (WSU) GeoAnalytical Lab for whole rock X-ray fluorescence (XRF) analyses. At Louisiana State University (LSU), these samples were cut and broken up to remove weathered surfaces and secondary chert veins and to obtain at least 100 grams of fresh material from each sample. Chips were handpicked at WSU and ground into a fine powder. The powders were mixed at a ratio of 2:1 with a di-lithium tetraborate flux and fused into glass beads in a muffle oven at 1000ºC. These glass beads were then reground, refused, thoroughly cleaned, and polished at 600 grit. This removes contaminant material from equipment and produces a flat surface for analysis. The sample beads were then loaded into WSU's ThermoARL Advant'XP+ sequential XRF spectrometer for analysis. This spectrometer is calibrated based on nine United States Geological Survey standard beads and two pure vein quartz standard beads. More detailed information on preparation and analysis methods, standards, and limits of detection is described by (Johnson et al., 1999) and can be found on the WSU GeoAnalytical Lab website (http://www.sees.wsu.edu/Geolab/index.html).

3.2. Handheld X-Ray Fluorescence

An Innov-X Systems Delta Mining Premium (DP 6000) handheld XRF device (Innov-X, 2010) was utilized for additional analyses in this study. Due to the potential inaccuracies of the instrument, a series of test analyses were performed on a number of samples that have been previously analyzed by bulk rock XRF at WSU using the procedures described in the previous section. These previous analyses were assumed to represent accurate values for the actual bulk

rock composition. The samples were chosen to represent high, median, and low compositions of major rock-forming elements as well as the immobile elements on which this study focuses (Al, Ti, Cr, and Zr). Through multiple sets of analyses and comparison to the previously obtained bulk rock analyses, it was determined that the device's "Soil Mode" provided the most accurate measurement of most elements. Unfortunately, Al is not measured in this mode and had to be measured using the less accurate "Mining+ Mode". A simple linear regression model was used to construct calibration curves based on the error observed in the known samples (Fig. 5). A data repository of test analyses with reported errors and calibrations is included in the Appendix.

Forty-one more Mendon samples were cut into slabs using an oil saw. These samples were selected to add supplemental data for some locations and to increase coverage to others. An additional sixteen samples were analyzed from the Weltevreden to determine if it is at all chemically correlative with the upper cycles of the Mendon. Four spots on each slab were targeted for analysis, avoiding weathered surfaces and chert veins, in order to best approximate bulk rock values. Each spot was analyzed using both the Soil Mode and Mining+ Mode of the device. Ti, Cr, and Zr values were obtained from the Soil Mode analyses, and Al values were obtained from the Mining+ Mode analyses. Al and Ti values, along with those for other major rock forming elements, were converted to wt % oxide and normalized to 100% on an anhydrous basis. All compositions were then calibrated using values calculated for each individual element during the test runs, and the four analyses for each sample were averaged.

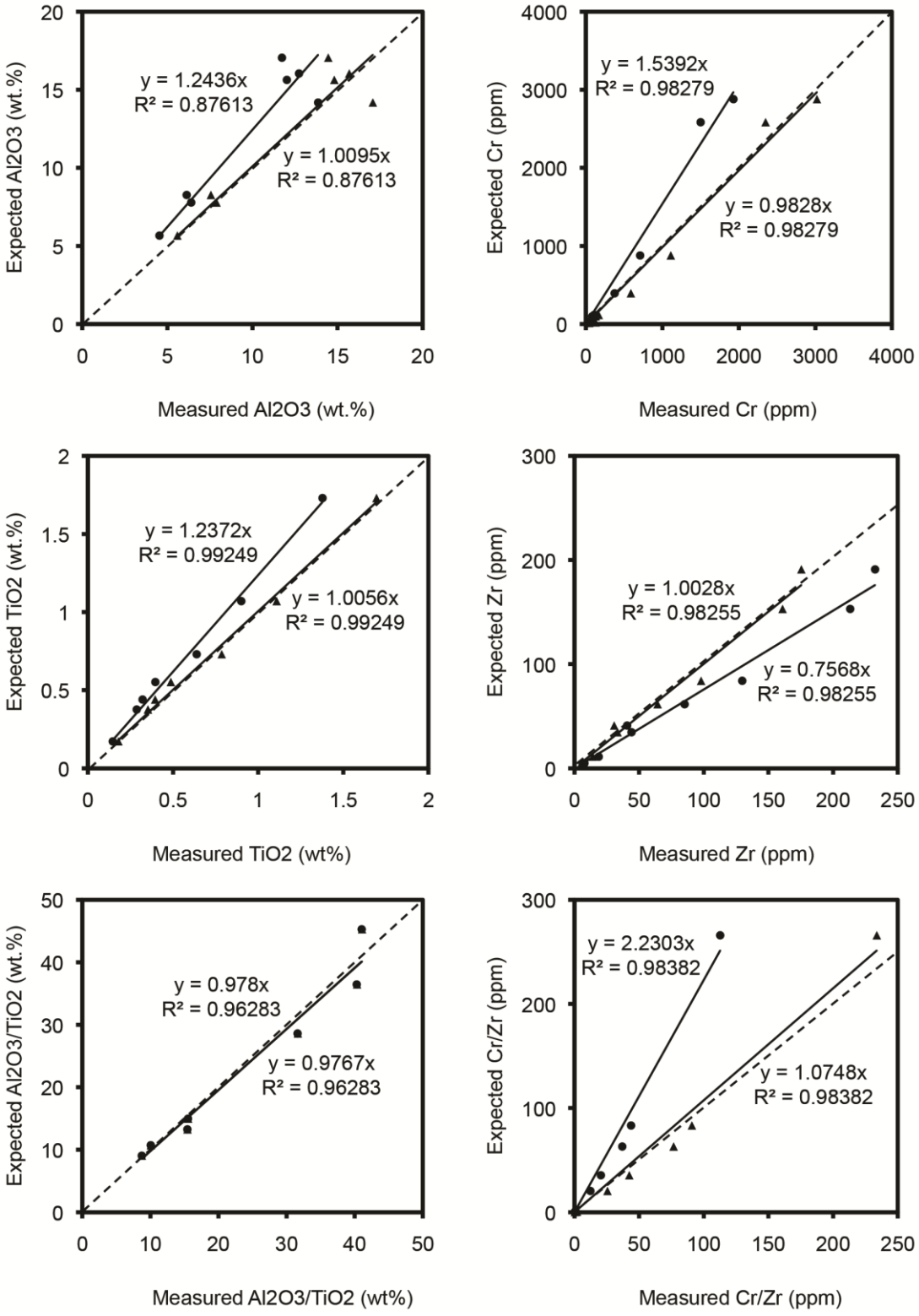

Figure 5. Calibration curves for Al2O3, TiO2, Cr, and Zr from handheld XRF. Dashed line represents unity between expected and measured values. More test data is in the Appendix.

3.3. Geochronology

Samples from seven different sections of upper Mendon and lower Fig Tree were chosen for sensitive high resolution ion microprobe-reverse geometry (SHRIMP-RG) analysis. Samples were broken up and weathered surfaces removed, resulting in approximately 1 kg of unprocessed material for each sample. Mineral separates were obtained from this material via standard separation techniques, including crushing, grinding, heavy liquids, and magnetic separation. Zircons were picked and mounted on 1" disks and then polished to reveal cross-sections. Analyses were performed at the SUMAC facility at Stanford following the methods of Premo et al. (2008). AS3 (Schmitz et al., 2003) and MAD were run as standards. Data reduction was accomplished using SQUID and ISOPLOT (Ludwig, 2001, 2003). Ages are calculated using ^{204}Pb-corrected ^{207}Pb/^{206}Pb ratios (hereafter referred to as Pb/Pb) and ^{204}Pb-corrected ^{206}Pb/^{238}U and ^{207}Pb/^{235}U concordia model ages (hereafter referred to as U/Pb).

4. Mendon Stratigraphy

Stratigraphic variation in the Mendon is controlled by facies change, especially across major faults, and other possible factors. The silicified tuff layers of the Mendon Formation are generally interpreted as distal pyroclastic fall units best described by Lithofacies I using the classification scheme of Thompson-Stiegler et al. (2011). In the lower Mendon, these fall layers are deposited as either single fall events on the order of 1 to 20 cm thick or stacked successions of multiple fall events that range from a few centimeters to tens of meters thick (Lowe, 1999c; Thompson-Stiegler et al., 2011). Individual fall events of sufficient thickness display well developed normal grading throughout and current-structuring in the finer ash at the top. This results in sharp contacts between the fine ash at the top of layers and the larger accretionary lapilli that mark the base of a new layer. Individual fall layers in the upper Mendon are similar to those lower in the section in terms of sedimentology and thickness, but the number of fall layers, maximum aggregate thickness of stacked fall events, and amount of current-structuring generally decrease up section. Successive layers in these sections reach no more than a few meters in thickness and are separated by several meters of black chert in the most expanded sections. Pyroclast and accretionary lapilli morphologies are similar to those described for the Mendon by Thompson-Stiegler et al. (2008, 2010, 2011) and Lowe (1999c). Flow units are found interbedded with these distinct tuffs in most localities. While most Mendon outcrops are well described by the depositional trends described previously, there are many exceptions. The two sections detailed here have specific local implications for Mendon volcanism and stratigraphy.

4.1. Umbaumba Gorge Section

Umbaumba Gorge between the Eucalyptus Mill and Auber Villiers faults (Fig. 2) is a section that extends from M3v into the basal rocks of the Fig Tree Group (Fig. 6). M3v is recorded here by at least 15 m of silicified komatiitic flows. It is possible that this represents the altered flow top and that the lower portions of this unit are preserved further down sections in areas not covered by this study. There are no pyroclasts recorded in the 1 m of black chert representing M3c. Another 37 m of less silicified komatiitic flow here defined as M3v2 conformably overlie this, followed by a few meters of black and black and white banded chert and several meters of banded ferruginous chert. Within the basal meter of black chert, there are fifty centimeters of distinctive tuff and accretionary lapilli. The base of this tuff layer is fine-grained and current-worked. The tuff is composed of abundant small, fluidly deformed glass shards and bubble wall fragments. Vesicles within the glass shards are stretched along one axis. A few fine-grained accretionary lapilli are contained within this section. The tuff directly above consists of larger glass shards that appear to have undergone more extensive fluid deformation during cooling (Fig. 4). From the shape of the vesicles, it appears as if these shards were stretched along one axis and then later curved along an axis perpendicular to the axis of elongation. Many shards contain relict “bridges” where two shards might have been initially connected and were pulled apart as they cooled. The size of the shards increases up section, as does the degree of fluid deformation. These tuff layers are directly overlain by a few meters of black chert followed by forty meters of banded ferruginous chert and the S2 spherule layer.

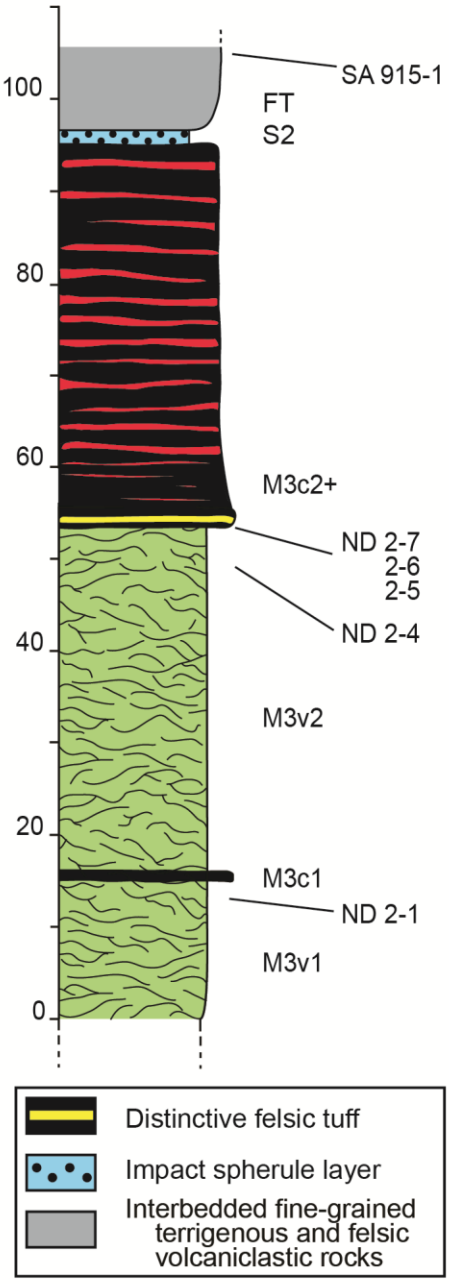

Figure 6. Stratigraphic column for the section at Umbaumba Gorge. Location ND 2 in Fig. 2.

4.2. The 620 Section

The 620 section is located north of the Kromberg Fault, near the Angle Station Syncline (Fig. 2), and is named for samples collected by Don Lowe from this location. It records one of the most complete sections of upper Mendon tuffs available. The section represented here extends from M2v into the lower Fig Tree (Fig. 7). Abundant komatiitic ash and accretionary lapilli are preserved here but records no interbedded lava flows. It contains a few interbedded banded ferruginous cherts, which likely represent lateral equivalents of the lava flows (Lowe, 1999b). The base of the section is not preserved. Just below the section in this location, there is a steep valley filled with dense vegetation.

The base of what is exposed consists of 4 m of black chert interbedded with massive, very fine grained grey ashes. This is overlain by 4 m of banded ferruginous chert that is likely the lateral equivalent of M2v and approximately 8 m of capping chert with a basal, 1 m thick tuff layer. This tuff layer displays crossbedding and discontinuous, lenticular layers of accretionary lapilli suspended in black chert at its top. The following 20 m of banded ferruginous chert is interpreted as the lateral equivalent of M3v and is the last evidence of a lava flow deposited into this basin. The remaining 43 m of section consists of individual fall units <10 cm thick in three distinct stacks between 1 – 4 m thick that are each interbedded with >10 m of black chert and very fine, massive tuff. These fall units contain many distinctive accretionary lapilli and represent chert layers from M3c to M5c. The deposits of M3c show periods of quiescence between multiple pyroclastic episodes. M4 volcanism is not recorded here. While fall units have not been previously recognized in M5, the uppermost Mendon tuff in this section is interpreted to be part of M5c. The S2 spherule layer directly overlies this. A few small layers of reworked komatiitic ash and sand are deposited 2 m above the spherule bed.

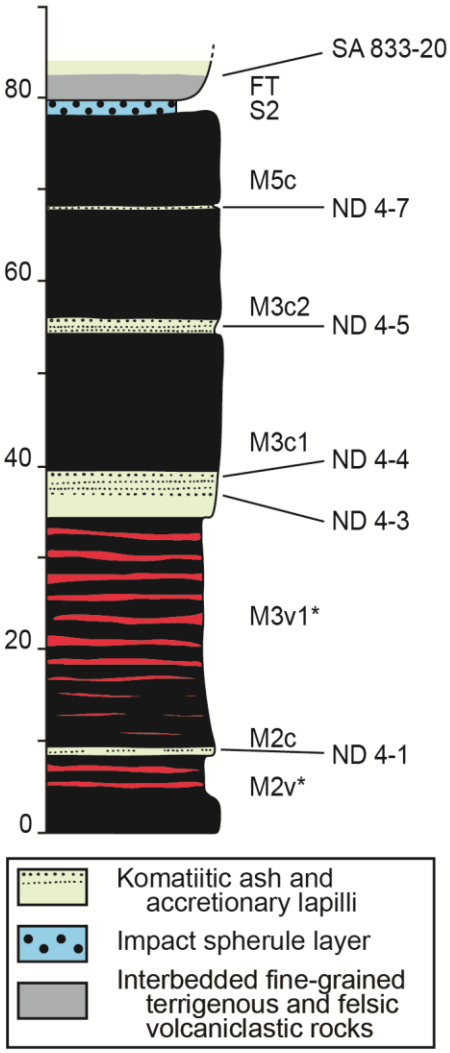

Figure 7. Stratigraphic column for the “620” section. Location ND 4 and SA 833 in Fig. 2.

5. Geochemistry

5.1. Bulk Rock X-Ray Fluorescence

As a result of pervasive post-depositional silicification, bulk compositions of all Mendon volcaniclastic units and nearly all Mendon flow rocks analyzed in this study are dominated by SiO_2, Al_2O_3, and K_2O, similar to findings of previous studies (Duchac and Hanor, 1987; Hanor and Duchac, 1990; Hofmann, 2005). They are depleted in virtually all other mobile elements. Immobile elements may even be depleted to some degree in more extensively silicified samples, especially tuffs with high initial porosities (Rouchon and Orberger, 2008). It is more useful to focus on the ratios of immobile elements, which are the only values shown to be consistent throughout units (Hofmann and Harris, 2008), when making correlations based on geochemistry. This study focuses on $Al2O_3/TiO_2$ and Cr/Zr, as they appear to be most distinctive in Mendon units. The bulk rock XRF analyses presented here fit into six distinct Al_2O_3/TiO_2 vs. Cr/Zr compositional fields (Fig. 8). While five of the six fields define unique units or successions of units, one of these fields is the product of overlap between the compositional ranges of M2v, M3c, M3v, and flows from higher sections of M4v. Additional lines of evidence are necessary to accurately correlate samples that fall into this indistinct compositional field. Stratigraphic relationships and distinctive textural features have been used where available.

While results of these analyses (Tables 1, Fig. 8) are mostly consistent with predictions based on field observations of stratigraphic relationships, a number of analyses identify units not previously observed in the Mendon. Tuffs from both the 620 Section and Maid of the Mists Mountain plot within the unique compositional field of M5v. A tuff in a chert capping M3v at the Umbaumba Gorge section, initially described as a komatiitic tuff based on hand sample and thin section, is identified as a felsic tuff based on its low Cr/Zr ratio. In the 620 section, the

Table 1: Bulk rock XRF major and trace element abundances for Mendon samples

Sample:	ND 1-1	ND 1-4	ND 1-5	ND 2-1	ND 2-4	ND 2-5	ND 2-6	ND 2-7	ND 4-1	ND 4-3	ND 4-4
Member:	FT	M5c+	M3c2	M3v1	M3v2	M3c2	M3c2	M3c2	M2c	M3c1	M3c1
Lat**:	52.783'	52.783'	54.067'	54.067'	54.067'	54.067'	54.067'	54.067'	52.783'	52.783'	52.783'
Long**:	04.850'	04.850'	00.317'	00.317'	00.317'	00.317'	00.317'	00.317'	04.850'	04.850'	04.850'
Normalized major element oxides (wt.%)											
SiO2	97.18	97.03	93.42	89.79	76.00	93.71	94.13	93.30	94.66	89.64	90.01
TiO2	0.052	0.193	0.100	0.399	0.376	0.218	0.180	0.244	0.242	0.502	0.535
Al2O3	1.51	2.28	5.15	6.00	17.05	4.48	3.92	4.68	2.43	7.48	7.30
FeO*	0.37	0.04	0.11	1.07	0.58	0.13	0.32	0.21	1.44	0.19	0.13
MnO	0.005	0.001	0.000	0.026	0.003	0.001	0.001	0.001	0.005	0.001	0.001
MgO	0.26	0.04	0.09	0.74	0.67	0.11	0.23	0.16	0.86	0.23	0.16
CaO	0.35	0.01	0.02	0.24	0.01	0.00	0.05	0.01	0.01	0.07	0.04
Na2O	0.00	0.01	0.03	0.07	0.19	0.04	0.03	0.04	0.00	0.04	0.05
K2O	0.27	0.39	1.07	1.67	5.10	1.29	1.08	1.32	0.33	1.78	1.73
P2O5	0.005	0.005	0.022	0.005	0.017	0.013	0.054	0.025	0.022	0.072	0.049
Trace Elements (ppm)											
Ni	270.3	22.9	27	451.7	67.4	4.6	8.5	6.1	74.4	91.1	56.1
Cr	877.5	393.2	21.4	2265.8	2879.3	10	10.7	7.9	174.8	147.1	69.2
Sc	6.9	4.2	2.7	23.6	42.4	6.5	6	6.9	2.8	10.7	12.2
V	36.9	65.9	14.3	166.6	246.9	7.9	5.5	3.6	59.4	142.2	142.9
Ba	17295.2	11388.4	9048.5	143.3	786	348	276.2	357.5	288.1	3123.5	3135.1
Rb	7.1	10.6	29.5	41.5	127.1	30.4	25.9	31.2	12.1	63.4	60.8
Sr	134.3	34	23.7	4.2	7.9	2.7	4.2	4.5	11.5	54.7	56.4
Zr	3.3	11.1	61.5	20.6	34.6	126	103	130.7	11.1	40.2	55.8
Y	1.2	2	10.7	3.6	5.4	25.7	19.3	19.6	3.3	8	13.5
Nb	1.5	1.8	5.2	1.1	2.3	6.5	5.6	7.9	2.5	3.9	3.4
Ga	1.5	3.5	6.3	7.1	11.6	6.2	4.9	6.5	4	9.2	9.6
Cu	5.5	28.4	3.6	63	3.8	0.9	1	1	52.1	86.5	100.8
Zn	4	2.3	0	17.9	0	0	0	0	0.5	0	0
Pb	3.1	2.3	2.4	1.3	1.1	1.6	2.2	1.7	16.9	4.8	3
La	0	0	14.3	0	2.1	9	8.4	10.9	8.9	15.3	11.6
Ce	0	0	21.6	3	4.4	15.4	23.8	21.3	20.7	25.2	14.8
Th	0	0.7	5.8	0.6	0.4	0.7	1.5	1.8	0.6	1.7	0.7
Nd	0	0	9.1	1.5	3.2	9.9	14.8	12.9	10.3	14.2	7.7
U	0	0.3	1.2	0	0.7	0	0.1	0	1.2	0.4	0
Immobile Element Ratios											
Al_2O_3/TiO_2	29.0	11.8	51.6	15.0	45.3	20.6	21.8	19.2	10.1	14.9	13.7
Cr/Zr	265.9	35.4	0.3	110.0	83.2	0.1	0.1	0.1	15.7	3.7	1.2

*Total iron as FeO.

**All latitudes are 25°S and all longitudes are 31°E

Table 1 continued

Sample:	ND 4-5	ND 4-7	ND 5-4 B	ND 5-4 A	ND 7-2	ND 7-3	SA 833 -13	SA 316 -6	SA 316 -4	SA 316 -3	SA 316 -1
Member:	M3c2	M5c	M3c2	M5c	M2c	M2c	M5c+	M3v2	M3v2	M5v	M5v
Lat**:	52.783'	52.783'	53.148'	53.148'	56.670'	56.670'	52.783'	54.933'	54.933'	54.933'	54.933'
Long**:	04.850'	04.850'	03.577'	03.577'	06.582'	06.582'	04.850'	03.100'	03.100'	03.100'	03.100'
Normalized major element oxides (wt.%)											
SiO2	90.81	95.60	86.34	91.95	95.38	95.47	98.33	88.60	67.06	76.09	74.11
TiO2	0.494	0.099	0.754	0.183	0.697	0.598	0.043	0.175	0.493	0.482	0.528
Al2O3	6.66	3.34	9.61	5.76	2.91	2.93	1.19	8.29	22.07	17.16	18.71
FeO*	0.14	0.11	0.23	0.23	0.14	0.06	0.11	0.14	0.82	0.49	0.47
MnO	0.001	0.000	0.001	0.001	0.002	0.001	0.002	0.001	0.005	0.000	0.000
MgO	0.16	0.06	0.21	0.12	0.02	0.02	0.03	0.23	1.67	0.41	0.70
CaO	0.04	0.00	0.00	0.00	0.09	0.04	0.03	0.00	0.00	0.00	0.00
Na2O	0.04	0.02	0.03	0.02	0.04	0.05	0.00	0.10	0.09	0.11	0.11
K2O	1.61	0.77	2.80	1.70	0.62	0.78	0.27	2.47	7.79	5.22	5.38
P2O5	0.049	0.011	0.021	0.033	0.089	0.061	0.003	0.002	0.005	0.037	0.010
Trace Elements (ppm)											
Ni	37.8	18	9.1	5.8	467.4	599.4	115.5	14.7	53	60.7	44.9
Cr	56.3	97.8	89.8	1397.2	1249.1	1448.3	642	1754.1	4846.2	1300.7	660.6
Sc	11.4	4	7.4	8.3	9.6	12.2	0.9	14.5	44.7	43.9	44.1
V	129.5	67.2	202	151.8	115.8	123.2	21.8	132.1	323.7	267	293.2
Ba	2629.2	2034.2	398.7	234	116.7	159.7	1664.8	1200.1	3975.5	4750.6	14772.2
Rb	53.5	24.3	98	61.4	16.7	23.3	10.4	52.4	199.5	123.7	112.9
Sr	55	22	17.6	25.9	18.9	18.5	3.8	5.6	4.4	17.5	11.6
Zr	51.9	4.8	32	23.5	39	36.4	1.2	20.4	50.8	29.1	32.5
Y	11.1	1.6	6.7	6	11.4	13.9	0.7	1.4	7.6	10.5	8.4
Nb	3.1	1.4	3.2	1.6	7.4	4.1	0.5	1.2	3.2	2	2.2
Ga	8.8	5.3	12.6	8.8	6	6.1	0.6	8	14.9	13.9	15.3
Cu	119.2	63.4	3.6	11.5	125.4	190.1	9	1.9	2.9	11.2	5.5
Zn	0	0	0.2	36.6	7.1	1.4	1.9	14	5.9	1.8	0
Pb	3.8	3.1	3	1.5	1.2	2.9	2.7	1.2	0.9	2.1	2.2
La	4.6	3.8	7.5	6.7	11.8	2.4	0.7	0.6	5.6	17.4	0
Ce	13.6	1.5	18.7	7.5	31.3	11.4	0	0	4.3	20.6	0
Th	0.5	0.7	0.6	1.8	0.8	0	0.1	0.4	0.5	1	0.3
Nd	6	1.1	8.1	4.4	17.8	9.2	1.6	0	0.2	22.1	0
U	0.1	0	0	0	0.3	0	0.3	0	0.5	0.1	0
Immobile Element Ratios											
Al_2O_3/TiO_2	13.5	33.7	12.7	31.5	4.2	4.9	28.0	47.3	44.8	35.6	35.5
Cr/Zr	1.1	20.4	2.8	59.5	32.0	39.8	535.0	86.0	95.4	44.7	20.3

*Total iron as FeO.

**All latitudes are 25°S and all longitudes are 31°E

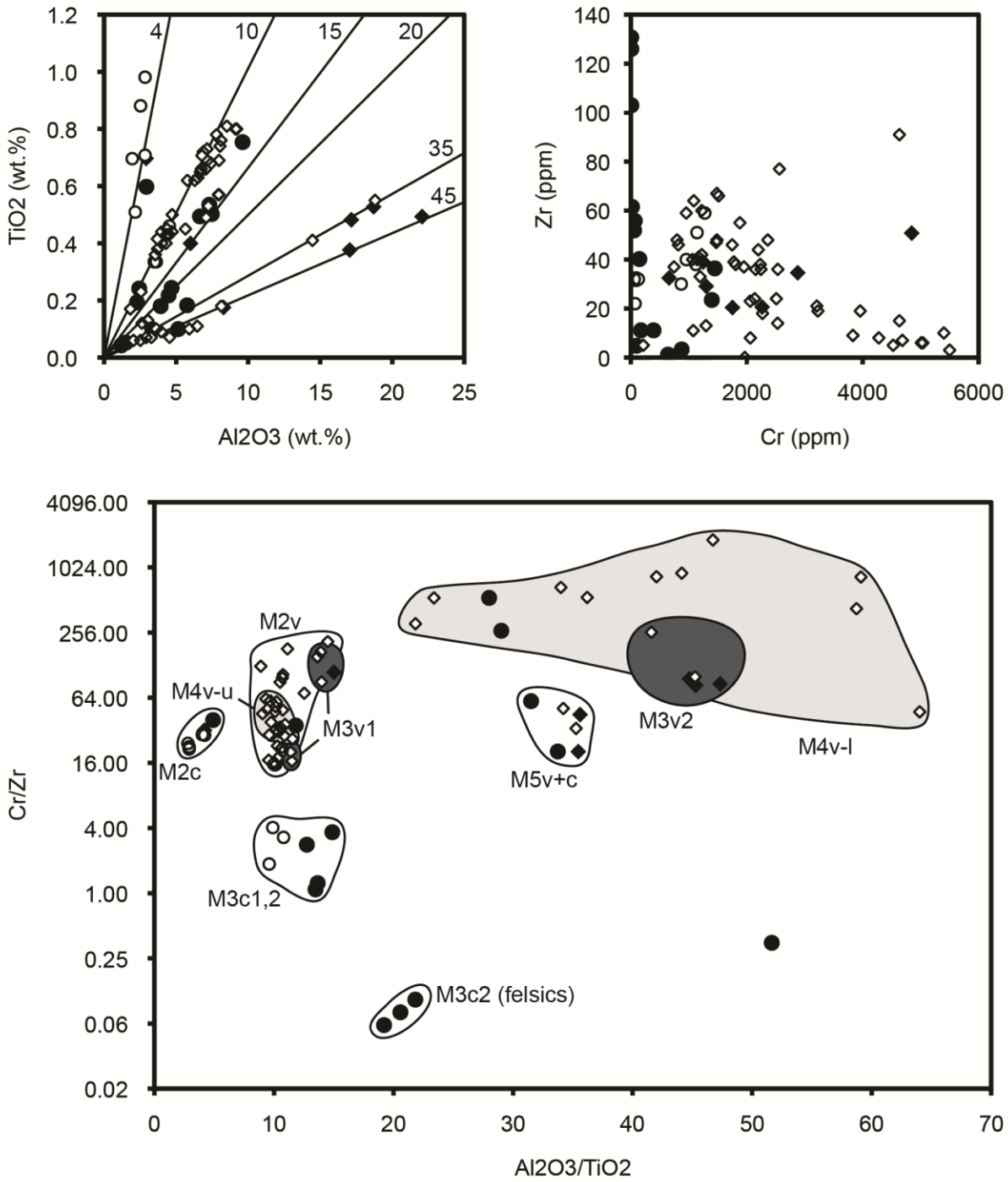

Figure 8. Variations in Al2O3, TiO2, Cr, and Zr from bulk rock analyses. Circles and diamond represent tuffs and flow rocks respectively. Solid shapes are newly analyzed samples, non-filled shapes are values from Byerly (1999) and Thompson-Stiegler et al. (2011). (top left) Lines represent common values for Mendon Al2O3/TiO2 ratios. (bottom) Fields represent common compositional fields for Mendon cycles.

capping chert above the banded ferruginous chert interpreted to be laterally equivalent to M2v contains a tuff that is compositionally similar to either M2v or M3 instead of M2c. All other analyses fall into the expected chemostratigraphic order except where a unit is absent.

5.2. Handheld X-Ray Fluorescence

Results from supplemental samples for the cluster of sections around where the Auber Villiers, Eucalyptus Mill, and Kromberg faults meet (Fig. 2) add increased resolution to chemical constraints for Mendon cycles. M2 through M5 are represented in these sections, and Al_2O_3/TiO_2 ratios from analyzed samples support this (Fig. 9 and Table 2). The majority of analyses are in agreement with previously observed chemostratigraphic relations; however, an expanded section of M2v's silicified zone contains flows with Al_2O_3/TiO_2 ratios of 19-23 and Cr/Zr ratios of ~100 interbedded with more expected values of 9-15 and ~40. All other analyses from this area yield results consistent with their location and stratigraphic height.

Sample locations outside of more well-studied areas and on the fringe of the Mendon's areal extent are represented here by a small number of analyzed samples. The small number of samples coupled with the large study area results in a lack of control on the correlations presented. These analyses should thus be considered a target for future research instead of constraint on stratigraphy. The Eastern Domain consists of areas between the Kromberg Fault and the Swaziland border and includes southwest-northeast trending bands of Mendon outcrops. Outcrops here likely represent a succession from M1 to M4 or M5; however, these bands are also likely the product of structural repetition, as they are tectonically juxtaposed with Fig Tree, Moodies, and other Mendon rocks. Sections appear to young to the northwest. Locations found on the opposite end of the West Central Domain, just south of the Inyoka Fault, are the northern-

most outcrops of the Mendon currently recognized. Samples from this area of the belt are sparsely distributed, and the stratigraphic height of these samples is ill-constrained. While the analyses for the samples are presented (Table 2), they are not put in stratigraphic context due to these poor controls.

The sixteen samples from the Weltevreden cover a wide areal extent and are somewhat distinct from the upper cycles of the Mendon (Fig. 9). The Al_2O_3/TiO_2 ratios of these samples falls within 16-19 and 22-29, which are similar ranges to others previously reported (Thompson-Stiegler et al., 2012). Compositions in these ranges are found within the Mendon, but the wide range of compositions seen in the Mendon is not seen here. The chemostratigraphic relations of the Weltevreden also do not correspond to those of the age-correlative upper Mendon.

Correlations based on these handheld analyses (Table 2) require additional caution and consideration beyond that needed for the bulk rock analyses. Repeated tests have shown that the errors reported by the device are not appropriate (Appendix). Systematic biases have been corrected for based on these tests, but the calibrations applied do not improve accuracy in every case. For this reason, correlations are made based on recognition of known chemostratigraphic patterns and not individual analyses. Further complications arise from sample heterogeneities and peak interference. The DP6000 integrates the composition of a spot on the order of a few centimeters instead of measuring the whole rock composition. If an element is preferentially partitioned into minerals like chrome spinel, pyrite, or zircon, it is possible that the spot analyzed by the device will give a skewed analysis due to concentration or absence of the enriched mineral. To compensate for this, four spots on each sample are analyzed and averaged to give an approximation of the bulk rock composition. Samples with largely heterogeneous analyses (those that deviate >25% from the average ratio) are excluded, but the potential for skewed analyses

Table 2: Average handheld XRF major and trace element abundances for Mendon Samples

Sample	Member	Latitude (S)	Longitude (E)	Al2O3	TiO2	Al_2O_3/TiO_2	Cr	Zr	Cr/Zr
SA 22-60*	M3v1	25°54.546'	31°02.713'	8.23	0.546	15.4	3540	31	115
SA 22-62	M3v2	25°54.546'	31°02.713'	18.78	0.440	43.3	4991	52	97
SA 56-1	M4v-l?	25°52.661'	30°56.745'	4.67	0.125	37.6	5720	10	572
SA 162-1	M5v	25°53.866'	31°02.534'	16.00	0.513	31.1	4854	131	37
SA 162-2	M5v	25°53.866'	31°02.534'	16.84	0.542	31.4	3939	139	28
SA 163-1	M3v1	25°54.285'	31°02.532'	6.62	0.456	14.7	2632	27	97
SA 163-2	M3v1	25°54.285'	31°02.532'	6.61	0.522	13.0	2714	26	106
SA 163-3	M3v1	25°54.285'	31°02.532'	8.16	0.583	14.0	2124	34	63
SA 226-5	M4v-l?	25°52.469'	30°56.956'	14.79	0.758	19.8	10131	27	386
SA 236-1	M5v?	25°52.917'	30°55.810'	13.72	0.418	33.7	894	24	36
SA 317-1	M3v2	25°54.084'	31°02.978'	12.91	0.293	44.1	2801	30	94
SA 317-2	M3v2	25°54.084'	31°02.978'	13.11	0.256	51.2	4145	29	143
SA 317-4	M3v2	25°54.084'	31°02.978'	10.93	0.270	40.7	2143	33	65
SA 317-5	M3v2	25°54.084'	31°02.978'	11.29	0.281	40.2	2082	31	67
SA 317-6	M3v1	25°54.084'	31°02.978'	7.63	0.528	14.4	3405	32	106
SA 330-1	M4v-u?	25°52.313'	31°00.380'	7.82	0.765	10.3	2227	39	57
SA 430-1	M4v-l	25°55.334'	31°03.157'	7.78	0.250	31.1	2003	33	65
SA 430-2	M4v-l	25°55.334'	31°03.157'	4.10	0.157	29.5	2324	21	121
SA 430-3	M4v-l	25°55.334'	31°03.157'	12.23	0.291	42.1	2139	30	71
SA 430-4	M5v	25°55.334'	31°03.157'	15.88	0.482	33.1	719	30	24
SA 614-3	M2v	25°54.306'	31°02.975'	7.24	0.498	14.6	2612	31	84
SA 614-4	M2v	25°54.306'	31°02.975'	2.68	0.209	14.0	960	15	68
SA 614-5	M2v	25°54.306'	31°02.975'	8.07	0.425	19.2	2718	21	138
SA 614-7	M2v	25°54.306'	31°02.975'	8.86	0.914	10.9	2205	54	44
SA 614-8	M2v	25°54.306'	31°02.975'	4.85	0.507	9.6	2353	43	57
SA 614-9	M2v	25°54.306'	31°02.975'	6.88	0.425	16.2	1861	19	100
SA 614-10	M2v	25°54.306'	31°02.975'	2.97	0.318	9.3	1119	21	54
SA 614-14	M2c	25°54.306'	31°02.975'	3.03	0.359	8.6	54	32	2
SA 614-22	M2v	25°54.306'	31°02.975'	7.26	0.344	21.0	2321	12	199
SA 614-23	M2v	25°54.306'	31°02.975'	9.86	0.431	23.0	2514	17	145
SA 614-24	M2v	25°54.306'	31°02.975'	7.73	0.638	12.2	2173	40	55
SA 614-26	M2v	25°54.306'	31°02.975'	3.59	0.342	10.5	1477	26	56
SA 757-1	M3v1	25°54.546'	31°02.713'	6.39	0.459	13.9	3194	28	113
SA 757-2	M3v2	25°54.546'	31°02.713'	10.66	0.267	40.0	3829	28	137
SA 757-3	M3c2	25°54.546'	31°02.713'	6.02	0.237	25.3	353	12	28
SA 809-2	M2v	25°55.849'	31°06.525'	2.60	0.344	7.7	1615	23	73
ND 6-2	M4v-u	25°53.823'	31°02.093'	8.06	0.926	8.8	5688	41	139
ND 6-2b	M4v-u	25°53.823'	31°02.093'	17.97	2.416	7.5	4243	124	34
ND 6-1*	M4v-u	25°53.800'	31°02.072'	13.20	1.510	8.7	4200	82	53
ND 6-3	M5v	25°53.772'	31°02.139'	15.27	0.409	37.8	116	32	4

*Average of 3 analyses.

All other samples are averaged based on 4 analyses.

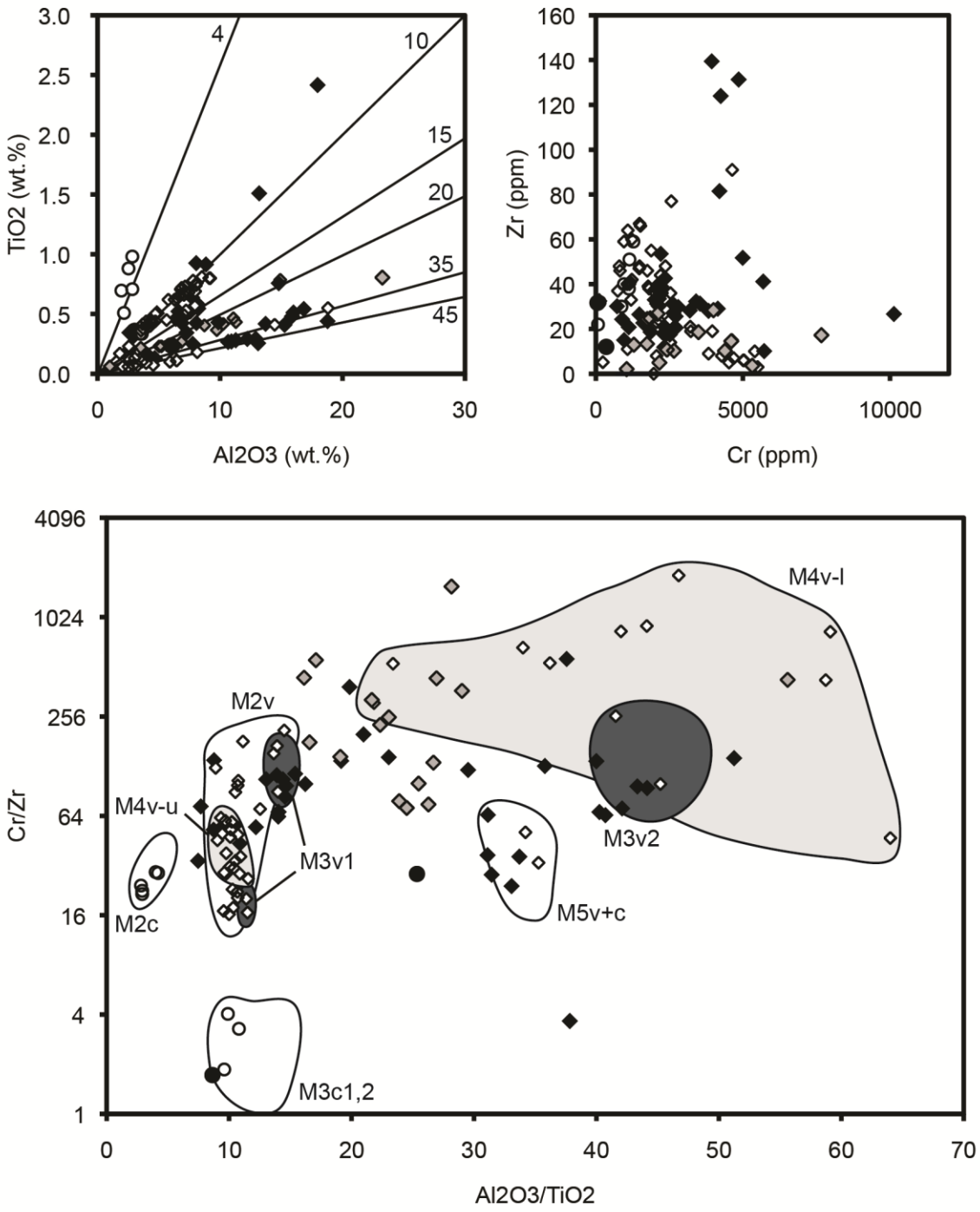

Figure 9. Variations in Al2O3, TiO2, Cr, and Zr from handheld analyses. Circles and diamond represent tuffs and flow rocks respectively. Solid shapes are newly analyzed Mendon samples, grey-filled shapes are newly analyzed Weltevreden samples, non-filled shapes are from Byerly (1999) and Thompson-Stiegler et al. (2011). (top left) Lines represent common values for Mendon Al2O3/TiO2 ratios. (bottom) Fields represent common compositional fields for Mendon cycles.

still exists. Interference between the Kα peak for Ti and the Lα peak for Ba has been confirmed to increase the measured amount of Ti by up to an order of magnitude in samples enriched in Ba (Appendix). This typically results in anomalously low Al_2O_3/TiO_2 ratios. Samples that might be enriched in Ba, come from localities known to be enriched in Ba, or were near layers of barite are thus excluded from consideration. Unfortunately, the device does not measure Ba contents of samples, so the possibility remains that some samples affected by this issue are have not been excluded; however, the absence of anomalously low Al_2O_3/TiO_2 ratios suggests that this is not the case. It is also likely that there are other interferences that have not been identified. These issues should be kept in mind when interpreting handheld XRF analyses. These numerous potential factors that could produce inaccurate analyses necessitate a cautious approach to correlation

5.3. Geochronology

Zircons derived from tuff and sandstone layers in seven sections were analyzed. Samples from four of these sections represent different units, and their ages are calculated individually. Samples from the remaining three sections were all collected from a tuffaceous green sand in M3c, and ages for zircons from these locations are presented as a single detrital population. The four individual samples analyzed (Table 3a and 3b, Fig. 10) are represented by populations of small (~100-150 μm), euhedral zircons. SA 907-5, collected from the Swaziland border in the Eastern Domain, is a fine-grained felsic ash from above M2c that appears to have been reworked by currents. Further up in section above M4c in the Barite Valley, SA 851-1 is a tuffaceous quartz-bearing sandstone ranging from fine grained-to-gravel sized. In the Fig Tree, an unusually crystal-rich tuff labeled SA 915-1 containing abundant quartz and sanidine (Fig. 4) was collected

Table 3a: U-Th-Pb SHRIMP-RG results for two Lower Fig Tree samples

Zircon #	% Common ^{206}Pb	U (ppm)	Th (ppm)	204corr 206Pb /238U Age (Ma)	1σ err (Ma)	204cor 207Pb /206Pb Age (Ma)	1σ err (Ma)	% Disc	238/ 206r	% err	207r /206r	% err	207r /235	% err	206r /238	% err	err Corr	Flags*
SA 833-20 (Lower Fig Tree tuffaceous sand)																		
2	0.10	493	213	2429.0	29.0	3112	5	28	2.18	1.4	.2388	0.3	15.07	1.5	.4576	1.4	.977	Reject
10	0.01	358	67	3088.0	35.4	3239	4	5	1.63	1.4	.2588	0.2	21.93	1.5	.6145	1.4	.988	
6	0.01	259	113	2880.0	34.1	3242	5	13	1.78	1.5	.2592	0.3	20.13	1.5	.5632	1.5	.981	
7	0.05	148	58	2696.7	34.5	3246	7	20	1.92	1.6	.2598	0.4	18.61	1.6	.5194	1.6	.967	
3	0.04	372	181	3063.6	35.3	3251	4	6	1.64	1.4	.2608	0.2	21.87	1.5	.6084	1.4	.986	
13	0.02	176	76	2824.0	34.5	3259	6	15	1.82	1.5	.2620	0.4	19.86	1.6	.5497	1.5	.968	
12	0.01	430	317	3200.3	36.3	3260	3	2	1.56	1.4	.2623	0.2	23.25	1.5	.6429	1.4	.990	
4	0.05	166	108	3006.2	36.5	3264	5	9	1.68	1.5	.2628	0.3	21.53	1.6	.5942	1.5	.975	
5	0.08	325	116	1984.6	24.8	3276	7	65	2.77	1.4	.2649	0.4	13.17	1.5	.3605	1.4	.957	
11	0.07	305	145	2395.1	29.0	3279	4	37	2.22	1.5	.2653	0.3	16.46	1.5	.4500	1.5	.983	
14	0.07	203	119	2749.1	33.3	3305	5	20	1.88	1.5	.2698	0.3	19.78	1.5	.5318	1.5	.977	Reject
15	0.00	136	81	3335.9	40.2	3368	6	1	1.48	1.5	.2809	0.4	26.25	1.6	.6778	1.5	.974	Reject
1	0.01	142	33	3503.1	41.4	3398	5	-3	1.39	1.5	.2863	0.3	28.50	1.6	.7219	1.5	.979	Reject
8	0.00	125	122	3416.0	41.3	3412	6	0	1.43	1.6	.2890	0.4	27.84	1.6	.6988	1.6	.973	Reject
9	0.02	191	115	3247.0	38.0	3427	4	6	1.53	1.5	.2917	0.3	26.33	1.5	.6548	1.5	.982	Reject
SA 915 (Lower Fig Tree dacitic tuff)																		
7	0.49	249	89	1992.0	25.3	2865	14	44	2.76	1.5	.2048	0.9	10.22	1.7	.3621	1.5	.860	Hi 204
8	0.05	136	110	3020.1	36.4	3240	7	7	1.67	1.5	.2589	0.4	21.33	1.6	.5976	1.5	.963	Discordant
3	0.06	117	83	2802.1	34.9	3242	6	16	1.84	1.5	.2593	0.4	19.46	1.6	.5445	1.5	.967	Discordant
2	0.02	50	44	3137.1	42.2	3256	8	4	1.60	1.7	.2615	0.5	22.60	1.8	.6268	1.7	.953	
14	0.11	21	6	3372.0	55.1	3261	13	-3	1.45	2.1	.2623	0.8	24.86	2.3	.6872	2.1	.928	
10	0.03	67	36	3174.0	41.1	3264	8	3	1.57	1.6	.2628	0.5	23.05	1.7	.6362	1.6	.959	
9	0.02	93	31	3360.9	41.1	3269	6	-3	1.46	1.6	.2637	0.4	24.88	1.6	.6843	1.6	.970	
4	0.01	121	57	3139.1	38.1	3274	6	4	1.59	1.5	.2646	0.4	22.88	1.6	.6274	1.5	.973	
12	0.03	36	19	3269.9	48.0	3276	14	0	1.51	1.9	.2649	0.9	24.13	2.1	.6607	1.9	.904	
13	0.02	87	47	3042.4	38.3	3298	7	8	1.66	1.6	.2686	0.4	22.33	1.6	.6031	1.6	.965	Discordant
5	0.09	231	179	2661.7	32.3	3319	10	25	1.96	1.5	.2723	0.7	19.19	1.6	.5112	1.5	.914	Discordant
1	0.07	358	395	2959.6	34.4	3350	31	13	1.72	1.4	.2776	2.0	22.30	2.4	.5827	1.4	.593	Reject
15	0.03	287	304	3130.8	36.0	3419	4	9	1.60	1.5	.2903	0.2	25.02	1.5	.6253	1.5	.987	Discordant
6	0.03	118	72	3108.4	37.7	3441	7	11	1.61	1.5	.2944	0.4	25.16	1.6	.6196	1.5	.960	Discordant
11	0.02	146	82	3360.1	39.6	3448	5	3	1.46	1.5	.2957	0.3	27.90	1.5	.6841	1.5	.980	Reject

*Flagged analyses are not used to calculate ages. All analyses with no flags are used in age calculations.

Table 3b: U-Th-Pb SHRIMP-RG results for two Mendon samples

Zircon #	% Common 206Pb	U (ppm)	Th (ppm)	204corr 206Pb /238U Age (Ma)	1σ err (Ma)	204cor 207Pb /206Pb Age (Ma)	1σ err (Ma)	% Disc	238/ 206r	% err	207r /206r	% err	207r /235	% err	206r /238	% err	err Corr	Flags*
SA 851-1 (M4c+ tuffaceous sand)																		
10	0.18	710	534	2167.2	26.1	2906	25	34	2.50	1.4	.2101	1.5	11.58	2.1	.3996	1.4	.675	Hi U
9	0.14	352	212	2754.6	32.2	3153	15	14	1.87	1.4	.2450	0.9	18.01	1.7	.5331	1.4	.834	Hi U
6	0.13	374	196	2499.4	30.1	3198	4	28	2.11	1.5	.2522	0.2	16.47	1.5	.4736	1.5	.986	Hi U
4	0.05	311	140	2580.0	30.5	3222	4	25	2.03	1.4	.2560	0.2	17.37	1.5	.4922	1.4	.987	Hi 204
8	0.05	364	196	3044.9	34.8	3232	5	6	1.66	1.4	.2576	0.3	21.44	1.5	.6037	1.4	.981	Hi U
12	0.24	314	149	2051.7	25.3	3235	4	58	2.67	1.4	.2580	0.3	13.33	1.5	.3747	1.4	.983	Hi 204
13	0.39	185	86	2430.4	30.2	3273	7	35	2.18	1.5	.2645	0.5	16.70	1.6	.4579	1.5	.954	
5	0.01	190	96	3210.7	37.3	3277	4	2	1.55	1.5	.2651	0.3	23.59	1.5	.6455	1.5	.982	
1	0.02	254	131	3037.4	35.8	3278	4	8	1.66	1.5	.2652	0.3	22.01	1.5	.6019	1.5	.985	
14	0.04	257	138	3296.8	38.1	3279	4	-1	1.50	1.5	.2654	0.2	24.43	1.5	.6676	1.5	.988	
11	0.00	161	75	3394.7	39.4	3284	5	-3	1.44	1.5	.2663	0.3	25.45	1.5	.6932	1.5	.978	
2	0.18	364	217	1934.6	24.2	3370	8	74	2.85	1.4	.2812	0.5	13.57	1.5	.3500	1.4	.939	Hi U
3	0.38	330	149	2195.8	26.8	3386	117	54	2.46	1.4	.2841	7.5	15.90	7.6	.4058	1.4	.189	
7	0.03	110	81	3289.3	39.5	3435	5	4	1.50	1.5	.2933	0.4	26.92	1.6	.6657	1.5	.974	Discordant
SA 907-5 (M2c+ dacitic tuff)																		
2	0.13	1274	528	1050.0	51.2	2348	19	124	5.65	5.3	.1502	1.1	3.66	5.4	.1769	5.3	.978	Hi U
1	0.31	845	629	1712.6	79.4	2566	12	50	3.28	5.3	.1709	0.7	7.17	5.3	.3043	5.3	.992	Hi U
3	0.01	313	131	3211.0	133.8	3227	5	0	1.55	5.3	.2567	0.3	22.85	5.3	.6456	5.3	.999	Reject
6	0.02	260	102	2710.2	117.1	3263	19	20	1.91	5.3	.2627	1.2	18.93	5.4	.5226	5.3	.974	
18	0.02	292	125	2933.8	124.7	3269	4	11	1.73	5.3	.2637	0.3	20.95	5.3	.5763	5.3	.999	Reject
24	0.03	202	99	2990.3	126.7	3270	5	9	1.69	5.3	.2638	0.3	21.47	5.3	.5902	5.3	.998	Hi 204
7	0.02	184	84	2953.0	125.5	3274	8	11	1.72	5.3	.2645	0.5	21.19	5.3	.5810	5.3	.995	
23	0.01	363	197	3044.4	128.2	3276	3	8	1.66	5.3	.2649	0.2	22.05	5.3	.6036	5.3	.999	
4	0.02	340	171	3081.4	130.9	3279	12	6	1.63	5.3	.2654	0.8	22.43	5.4	.6128	5.3	.990	
27	0.00	223	82	3174.5	132.8	3283	5	3	1.57	5.3	.2661	0.3	23.35	5.3	.6363	5.3	.999	
26	0.01	140	49	3121.5	131.2	3285	5	5	1.61	5.3	.2663	0.3	22.87	5.3	.6229	5.3	.998	
13	0.02	132	48	3137.5	131.8	3285	6	5	1.59	5.3	.2664	0.4	23.03	5.3	.6269	5.3	.998	
10	0.02	153	50	2981.5	126.5	3285	5	10	1.70	5.3	.2664	0.3	21.60	5.3	.5880	5.3	.998	
19	0.00	265	135	3177.5	132.7	3285	4	3	1.57	5.3	.2665	0.3	23.41	5.3	.6371	5.3	.999	
21	0.01	223	75	3288.6	136.3	3286	4	0	1.50	5.3	.2665	0.3	24.46	5.3	.6655	5.3	.999	
15	0.03	168	90	2953.4	125.6	3286	9	11	1.72	5.3	.2665	0.5	21.36	5.3	.5811	5.3	.995	
11	0.00	211	87	3183.6	133.0	3286	5	3	1.57	5.3	.2666	0.3	23.48	5.3	.6386	5.3	.998	

*Flagged analyses are not used to calculate ages. All analyses with no flags are used in age calculations.

Table 3b continued

Zircon #	% Common 206Pb	U (ppm)	Th (ppm)	204corr 206Pb /238U Age (Ma)	1σ err (Ma)	204cor 207Pb /206Pb Age (Ma)	1σ err (Ma)	% Disc	238/ 206r	% err	207r /206r	% err	207r /235	% err	206r /238	% err	err Corr	Flags*
SA 907-5 (M2c+ dacitic tuff)																		
9	0.23	194	88	3025.6	128.2	3287	18	9	1.67	5.3	.2667	1.2	22.02	5.4	.5990	5.3	.977	
12	0.00	212	78	3063.9	129.2	3287	5	7	1.64	5.3	.2667	0.3	22.37	5.3	.6085	5.3	.998	
20	0.02	202	83	3090.8	130.0	3287	4	6	1.63	5.3	.2668	0.3	22.63	5.3	.6152	5.3	.999	
22	0.01	265	123	2979.2	126.2	3290	4	10	1.70	5.3	.2672	0.2	21.65	5.3	.5875	5.3	.999	
17	0.02	253	101	3036.1	128.1	3291	4	8	1.66	5.3	.2674	0.3	22.18	5.3	.6016	5.3	.999	
25	0.02	177	64	3195.9	133.5	3293	6	3	1.56	5.3	.2677	0.4	23.69	5.3	.6418	5.3	.997	
14	0.01	217	90	2946.3	125.3	3294	5	12	1.73	5.3	.2679	0.3	21.40	5.3	.5794	5.3	.998	
16	0.00	242	98	3237.0	134.7	3294	4	2	1.53	5.3	.2679	0.3	24.10	5.3	.6523	5.3	.999	
5	0.01	175	52	3127.0	131.2	3294	4	5	1.60	5.3	.2680	0.3	23.07	5.3	.6243	5.3	.999	
8	0.02	170	58	3148.3	132.0	3298	5	5	1.59	5.3	.2687	0.3	23.33	5.3	.6297	5.3	.998	

*Flagged analyses are not used to calculate ages. All analyses with no flags are used in age calculations.

Table 4: Aggregate detrital zircon population U-Th-Pb SHRIMP-RG results for three M3c green sand samples

Zircon #	% Common 206Pb	U (ppm)	Th (ppm)	204corr 206Pb /238U Age (Ma)	1σ err (Ma)	204cor 207Pb /206Pb Age (Ma)	1σ err (Ma)	% Disc	238/ 206r	% err	207r /206r	% err	207r /235	% err	206r /238	% err	err Corr
SA 811 (M3c green sand)																	
1	0.05	184	80	3441.6	52.6	3416	7	-1	1.42	2.0	.2898	0.4	28.19	2.0	.7055	2.0	.976
2	0.00	146	54	3392.4	52.4	3395	6	0	1.44	2.0	.2858	0.4	27.29	2.0	.6926	2.0	.980
3	0.24	310	184	3158.3	48.5	3348	5	6	1.58	1.9	.2773	0.3	24.17	2.0	.6322	1.9	.987
4	0.08	478	226	3199.6	48.6	3614	4	13	1.56	1.9	.3294	0.2	29.19	1.9	.6427	1.9	.993
5	0.06	138	104	3430.8	53.3	3375	7	-2	1.42	2.0	.2822	0.4	27.34	2.0	.7027	2.0	.978
6	0.01	242	155	3393.1	51.7	3383	5	0	1.44	2.0	.2837	0.3	27.10	2.0	.6928	2.0	.986
7	0.62	403	245	2907.9	45.3	3256	5	12	1.75	1.9	.2616	0.3	20.56	2.0	.5700	1.9	.987
8	0.04	145	61	3397.9	52.7	3405	7	0	1.44	2.0	.2876	0.4	27.52	2.0	.6940	2.0	.978
9	0.07	95	65	3388.4	54.4	3415	8	1	1.45	2.1	.2896	0.5	27.61	2.1	.6915	2.1	.967
10	0.14	186	178	3394.9	52.2	3364	7	-1	1.44	2.0	.2802	0.5	26.78	2.0	.6932	2.0	.974
11	0.04	262	113	3435.3	52.1	3421	5	0	1.42	2.0	.2906	0.3	28.20	2.0	.7039	2.0	.987
12	0.00	134	61	3429.6	53.6	3424	7	0	1.42	2.0	.2911	0.5	28.19	2.1	.7024	2.0	.976
13	0.01	149	56	3425.4	53.3	3426	7	0	1.43	2.0	.2916	0.4	28.19	2.1	.7013	2.0	.978
14	0.07	235	113	3319.6	50.8	3415	5	3	1.48	2.0	.2895	0.3	26.89	2.0	.6736	2.0	.985
15	0.07	137	55	3369.2	52.5	3413	7	1	1.46	2.0	.2891	0.4	27.36	2.1	.6865	2.0	.976
16	0.08	91	47	3834.9	59.6	3663	7	-4	1.23	2.1	.3400	0.5	38.10	2.1	.8128	2.1	.973
17	0.13	295	273	3269.0	49.9	3372	7	3	1.51	1.9	.2816	0.4	25.65	2.0	.6605	1.9	.975
18	0.19	163	67	3404.2	52.7	3402	6	0	1.44	2.0	.2870	0.4	27.53	2.0	.6957	2.0	.979
19	0.21	466	256	2251.0	36.7	3004	6	33	2.39	1.9	.2231	0.3	12.86	2.0	.4179	1.9	.985
20	0.06	150	111	3920.6	58.5	3811	7	-3	1.19	2.0	.3748	0.4	43.26	2.0	.8371	2.0	.976
21	0.05	119	83	3575.2	55.6	3531	7	-1	1.35	2.0	.3120	0.5	31.89	2.1	.7413	2.0	.976
22	0.03	190	69	3471.6	53.1	3415	6	-2	1.40	2.0	.2895	0.4	28.48	2.0	.7135	2.0	.983
24	0.02	233	103	3454.5	52.5	3409	5	-1	1.41	2.0	.2884	0.3	28.19	2.0	.7090	2.0	.985
25	0.06	126	56	3454.6	53.8	3398	7	-2	1.41	2.0	.2864	0.5	27.99	2.1	.7090	2.0	.976
26	0.13	81	62	3445.9	55.6	3378	9	-2	1.42	2.1	.2827	0.6	27.55	2.2	.7067	2.1	.963
27	0.08	175	73	3446.5	52.9	3415	6	-1	1.41	2.0	.2895	0.4	28.21	2.0	.7068	2.0	.982
28	0.02	151	59	3465.7	53.5	3411	6	-2	1.40	2.0	.2888	0.4	28.35	2.0	.7119	2.0	.980
29	0.48	526	501	2518.4	40.2	3185	6	26	2.09	1.9	.2501	0.4	16.48	2.0	.4780	1.9	.981
30	0.10	255	111	3029.5	47.2	3347	5	10	1.67	2.0	.2772	0.3	22.93	2.0	.5999	2.0	.985
31	0.22	93	65	3243.8	52.4	3380	9	4	1.53	2.1	.2832	0.6	25.53	2.1	.6540	2.1	.965
32	0.05	171	71	3439.6	53.0	3401	6	-1	1.42	2.0	.2869	0.4	27.89	2.0	.7050	2.0	.980
33	0.06	76	46	3499.4	56.7	3400	9	-3	1.39	2.1	.2868	0.6	28.51	2.2	.7209	2.1	.963
34	0.03	148	53	3464.8	53.7	3423	7	-1	1.41	2.0	.2911	0.4	28.56	2.1	.7117	2.0	.978

Table 4 continued

Zircon #	% Common 206Pb	U (ppm)	Th (ppm)	204corr 206Pb /238U Age (Ma)	1σ err (Ma)	204cor 207Pb /206Pb Age (Ma)	1σ err (Ma)	% Disc	238/ 206r	% err	207r /206r	% err	207r /235	% err	206r /238	% err	err Corr
SA 514 (M3c green sand)																	
8	1.98	1263	798	789.8	3.3	2803	25	255	7.67	0.4	.1972	1.6	3.54	1.6	.1303	0.4	.276
17	0.13	231	121	3529.2	18.1	3393	5	-4	1.37	0.7	.2854	0.3	28.68	0.7	.7289	0.7	.892
16	0.13	223	248	2633.7	14.7	3297	11	25	1.98	0.7	.2684	0.7	18.68	1.0	.5046	0.7	.701
18	0.00	255	80	3792.1	18.4	3700	9	-2	1.25	0.6	.3484	0.6	38.47	0.9	.8008	0.6	.742
20	0.06	77	47	3322.8	25.6	3395	8	2	1.48	1.0	.2859	0.5	26.59	1.1	.6744	1.0	.886
9	0.58	233	338	2145.4	20.8	3360	14	57	2.53	1.1	.2795	0.9	15.22	1.5	.3949	1.1	.786
10	0.06	221	134	3694.0	18.6	3520	6	-5	1.29	0.7	.3097	0.4	33.04	0.8	.7736	0.7	.861
28	0.05	156	101	3637.3	20.0	3682	11	1	1.32	0.7	.3443	0.7	35.99	1.0	.7581	0.7	.715
30	0.02	213	86	3410.1	16.2	3411	6	0	1.43	0.6	.2888	0.4	27.77	0.7	.6972	0.6	.840
34A	1.01	289	159	2516.8	12.1	3288	7	31	2.09	0.6	.2669	0.4	17.57	0.7	.4776	0.6	.798
37	0.14	253	165	3085.2	13.9	3402	5	10	1.63	0.6	.2870	0.3	24.29	0.6	.6138	0.6	.877
41	0.04	165	115	3360.4	18.4	3403	6	1	1.46	0.7	.2873	0.4	27.10	0.8	.6842	0.7	.891
43	0.25	311	205	3306.5	14.2	3308	6	0	1.49	0.5	.2703	0.4	24.98	0.7	.6702	0.5	.819
45	0.02	79	38	3654.1	28.9	3713	7	2	1.31	1.0	.3513	0.5	36.94	1.1	.7627	1.0	.911
46	0.03	215	215	3249.4	15.7	3404	5	5	1.53	0.6	.2876	0.3	25.99	0.7	.6554	0.6	.888
50	0.03	204	85	3394.0	16.8	3390	5	0	1.44	0.6	.2849	0.3	27.22	0.7	.6930	0.6	.892
51	0.84	307	634	2333.7	10.8	3264	6	40	2.29	0.6	.2629	0.4	15.81	0.7	.4362	0.6	.803
53	0.05	123	144	3152.3	20.9	3373	9	7	1.59	0.8	.2818	0.6	24.51	1.0	.6307	0.8	.826
56	0.02	192	70	3423.5	17.9	3400	5	-1	1.43	0.7	.2868	0.3	27.71	0.8	.7007	0.7	.894
57	0.04	179	251	3384.6	18.6	3376	6	0	1.45	0.7	.2824	0.4	26.88	0.8	.6905	0.7	.889
61	0.12	247	152	3182.2	14.9	3388	5	6	1.57	0.6	.2845	0.3	25.04	0.7	.6383	0.6	.871
63	0.00	170	97	3406.1	19.0	3419	6	0	1.44	0.7	.2902	0.4	27.85	0.8	.6962	0.7	.893
64	0.77	204	576	2859.4	14.9	3359	7	17	1.79	0.6	.2793	0.5	21.50	0.8	.5583	0.6	.808
66	0.14	86	41	3386.0	25.3	3416	8	1	1.45	1.0	.2897	0.5	27.59	1.1	.6909	1.0	.883
67	0.02	126	55	3505.4	21.6	3443	6	-2	1.38	0.8	.2948	0.4	29.37	0.9	.7225	0.8	.898
73	0.00	99	49	3407.8	23.6	3462	7	2	1.44	0.9	.2985	0.4	28.67	1.0	.6966	0.9	.897
74	0.03	202	77	3358.4	16.6	3397	5	1	1.46	0.6	.2863	0.3	26.98	0.7	.6837	0.6	.890
74A	0.04	220	285	3129.6	14.9	3372	5	8	1.60	0.6	.2816	0.3	24.26	0.7	.6249	0.6	.885
76	0.02	224	92	3336.7	17.9	3428	5	3	1.47	0.7	.2919	0.3	27.29	0.7	.6780	0.7	.915
85	0.05	76	52	3468.3	27.7	3456	8	0	1.40	1.0	.2973	0.5	29.21	1.2	.7126	1.0	.896
86	0.08	134	61	3413.3	20.5	3389	6	-1	1.43	0.8	.2847	0.4	27.40	0.9	.6981	0.8	.888
82	0.25	308	323	3465.7	14.0	3717	4	7	1.40	0.5	.3524	0.3	34.59	0.6	.7119	0.5	.900
89A	0.03	126	66	3278.8	20.5	3393	6	3	1.51	0.8	.2854	0.4	26.09	0.9	.6630	0.8	.887
90	0.00	147	63	3435.2	19.9	3413	6	-1	1.42	0.7	.2891	0.4	28.05	0.8	.7038	0.7	.896
92	0.35	266	312	2973.6	13.8	3410	5	15	1.71	0.6	.2886	0.3	23.32	0.7	.5861	0.6	.866

Table 4 continued

Zircon #	% Common 206Pb	U (ppm)	Th (ppm)	204corr 206Pb /238U Age (Ma)	1σ err (Ma)	204cor 207Pb /206Pb Age (Ma)	1σ err (Ma)	% Disc	238/ 206r	% err	207r /206r	% err	207r /235	% err	206r /238	% err	err Corr
SA 22 (M3c green sand)																	
1	2.21	144	128	3064.4	18.9	3367	11	10	1.64	0.8	.2807	0.7	23.55	1.0	.6086	0.8	.739
2	0.00	92	88	3449.5	24.4	3429	10	-1	1.41	0.9	.2921	0.6	28.50	1.1	.7076	0.9	.824
3	0.31	87	53	3379.0	24.1	3451	8	2	1.45	0.9	.2963	0.5	28.15	1.1	.6891	0.9	.863
4	0.13	43	72	3402.8	37.8	3375	12	-1	1.44	1.4	.2822	0.8	27.06	1.6	.6953	1.4	.879
5	4.88	193	77	2399.2	13.9	3467	12	45	2.22	0.7	.2995	0.8	18.62	1.0	.4509	0.7	.669
6	0.74	142	64	2983.2	18.5	3429	8	15	1.70	0.8	.2921	0.5	23.70	0.9	.5885	0.8	.818
7	3.99	160	70	2785.7	17.0	3434	12	23	1.85	0.8	.2932	0.8	21.85	1.1	.5405	0.8	.707
8	0.44	148	138	3555.4	21.4	3673	7	3	1.36	0.8	.3422	0.4	34.72	0.9	.7359	0.8	.876
10	0.96	55	18	3409.1	35.5	3547	13	4	1.43	1.3	.3154	0.8	30.30	1.6	.6970	1.3	.855
11	0.12	124	54	3406.0	23.2	3412	8	0	1.44	0.9	.2890	0.5	27.74	1.0	.6961	0.9	.876
12	0.21	124	102	3342.2	22.6	3384	8	1	1.47	0.9	.2838	0.5	26.58	1.0	.6794	0.9	.867
13	0.50	141	54	3346.9	22.4	3401	9	2	1.47	0.9	.2870	0.6	26.93	1.0	.6807	0.9	.836
14	0.63	110	119	3069.4	22.8	3396	10	11	1.64	0.9	.2860	0.6	24.05	1.1	.6098	0.9	.834
15	0.04	90	36	3447.3	26.7	3400	8	-1	1.41	1.0	.2868	0.5	27.96	1.1	.7071	1.0	.881
16	3.97	118	133	3158.3	22.5	3375	13	7	1.58	0.9	.2821	0.9	24.59	1.2	.6322	0.9	.721
17	3.92	126	81	3492.9	24.0	3566	11	2	1.39	0.9	.3192	0.7	31.65	1.1	.7192	0.9	.785
18	4.75	96	94	2875.0	24.5	3405	17	18	1.78	1.1	.2876	1.1	22.29	1.5	.5620	1.1	.690
19	0.71	67	38	3727.0	33.2	3727	10	0	1.28	1.2	.3546	0.6	38.27	1.3	.7828	1.2	.881
20	0.54	147	73	3063.2	18.9	3415	8	11	1.64	0.8	.2896	0.5	24.29	0.9	.6083	0.8	.844
21	0.96	150	61	3063.4	24.4	3403	11	11	1.64	1.0	.2873	0.7	24.10	1.2	.6084	1.0	.822
22	0.77	60	54	3329.5	41.8	3400	16	2	1.48	1.6	.2867	1.0	26.73	1.9	.6761	1.6	.845
23	0.25	143	52	3458.7	27.8	3386	9	-2	1.41	1.0	.2841	0.6	27.82	1.2	.7101	1.0	.869
24	0.44	130	51	3330.5	23.0	3541	8	6	1.48	0.9	.3140	0.5	29.29	1.0	.6764	0.9	.874
25	0.02	148	50	3392.8	21.8	3421	7	1	1.44	0.8	.2907	0.4	27.76	0.9	.6927	0.8	.879
26	1.37	103	85	3530.9	26.9	3620	9	3	1.37	1.0	.3306	0.6	33.24	1.2	.7293	1.0	.851
27	0.78	100	69	3267.3	25.9	3382	10	4	1.52	1.0	.2834	0.7	25.79	1.2	.6600	1.0	.838
30	0.05	50	27	3309.8	37.6	3428	13	4	1.49	1.5	.2920	0.8	27.01	1.7	.6710	1.5	.874
32	7.87	106	84	3431.5	29.4	3522	19	3	1.42	1.1	.3102	1.2	30.06	1.7	.7029	1.1	.668

10 m above the S2 spherule bed in the Umbaumba Gorge section; however, it is possible that this 10 m separation is the result of structural repetition. SA 833-20, a tuffaceous quartz-bearing sandstone, was collected 3 m above S2 in the 620 section. The zircons in the aggregate detrital population generally look less euhedral and more rounded, but are roughly equivalent in size to the more euhedral presented populations above. This population is derived from fine-grained tuffaceous green sandstone samples from SA 22, SA 514, and SA811, many of which contain accretionary lapilli. All samples analyzed contain abundant altered volcanic quartz.

All zircons analyzed from 907-5 represent a single population (Table 3b). Two of the 27 zircons were flagged, because they fell just outside of the age range defined by the rest of the zircons. An additional two zircons were flagged due to high U and a third for high ^{204}Pb. These zircons were excluded from age determinations. Calculations based on the remaining 22 zircons give a nicely concordant U/Pb age of 3287.3 ± 2.9 Ma and a nearly identical Pb/Pb age (Fig 10). The error ellipses for these data points are unusually elongate due to errors from the 204-corrected ^{206}Pb/^{238}U age that are about an order of magnitude higher than those in the Pb/Pb age. It is unknown exactly what the source of these errors is, but the ages are nonetheless concordant and define an expected Mendon Formation age in agreement with previous age determinations for the Mendon (Fig. 1).

Two populations of zircons were recognized in SA 851-1, a xenocrystic population and a younger population that was used in the age calculations. Seven other grains were also not used. Five of these were flagged due to high U and the remaining two due to high ^{204}Pb. The six zircons were used define a concordant age of 3279.8 ± 9.1 Ma and a nearly identical Pb/Pb age (Fig. 10). This age also falls within Mendon age constraints.

SA 915-1 is represented by at least two age populations. A large xenocrystic population

of five zircons has been excluded from age determinations. A potential younger population is likely the result of slightly elevated U and a zircon enriched in ^{204}Pb. The remaining zircons yield an average U/Pb age of 3267.8 ± Ma and a slightly younger Pb/Pb age (Fig. 10). These ages are in good agreement with previous age determinations for the base of the Fig Tree (Fig. 1).

Zircons from SA 833-20 are also split into two populations, one of which shows relatively elevated U contents (Table 3a). The xenocrystic population yields lower U contents than the population used to date this sample. The U/Pb age calculated from these zircons, 3261 ± 18 Ma, has a much larger error as a result. The Pb/Pb age calculated falls within error of this but has much smaller errors. These ages are still very reasonable for basal Fig Tree samples.

The aggregate detrital population is defined by a number of populations, including numerous xenocrystic populations (Table 4). While there is a wide spread of xenocryst ages, the spikes appear to occur at 3700 Ma, 3550 Ma, and 3400 Ma (Fig. 10). The maximum depositional age is interpreted to be 3308 ± 6, as this represents the first zircon with both relatively low U and ^{204}Pb contents that is less than 25% discordant.

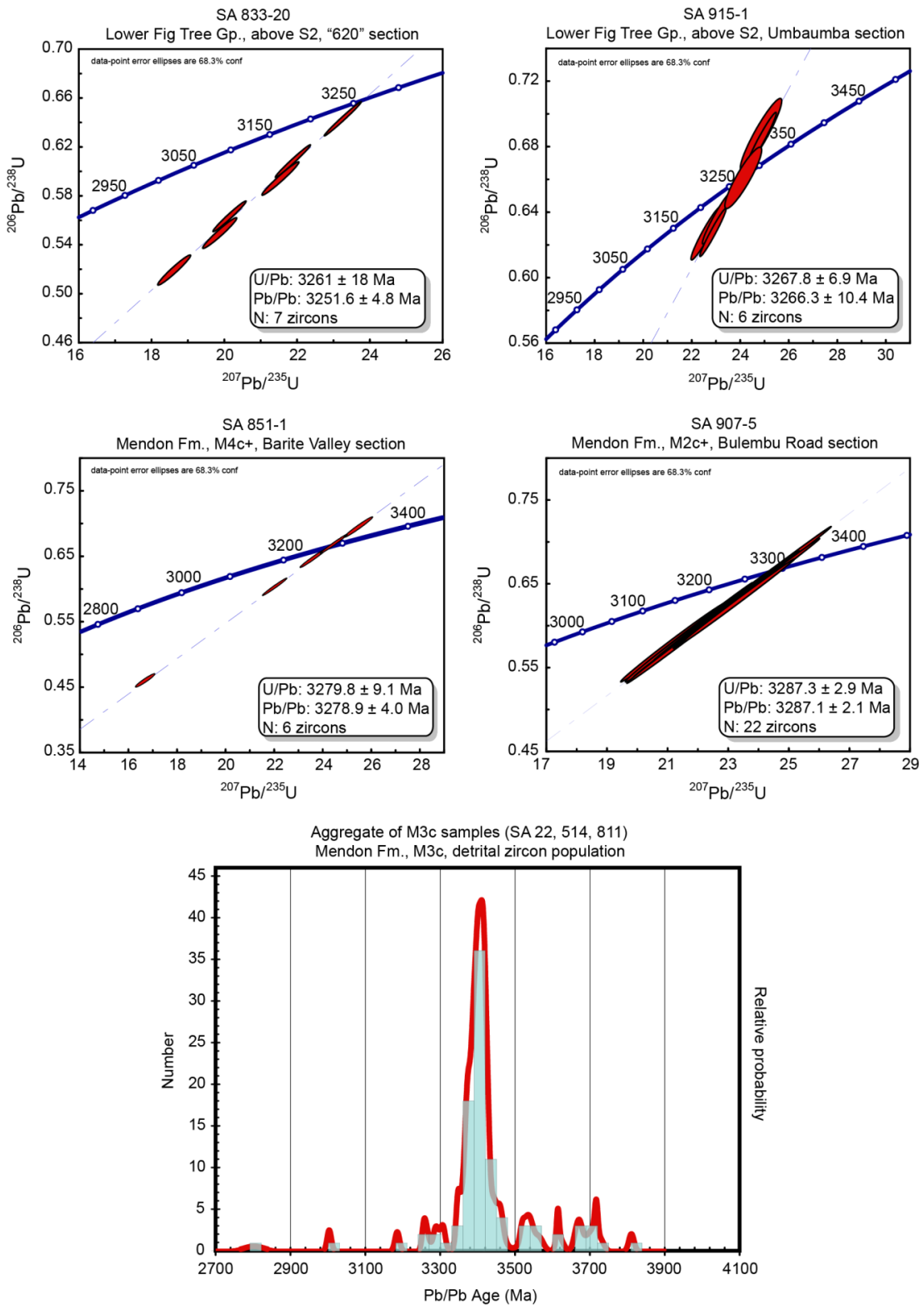

Figure 10. (top) Concordia plots for various Mendon and Fig Tree tuffs and sandstones. (bottom) Pb/Pb age distribution diagram for an aggregate detrital zircon population derived from multiple M3c sandstone samples.

6. Discussion

6.1. Chemostratigraphy

The results presented here aide in the creation of a chemical and stratigraphic framework for the Mendon Formation across its exposed chronological and spatial extent (Fig. 11). This framework is applicable across structure and facies change. With careful consideration, a section of Mendon can be correlated with existing stratigraphies solely based on the stratigraphic relations of chemically distinct units. Units with previously unrecognized (M5c) or indistinct compositions (M2v, M3v+c, M4v) can easily be placed into this framework using observations of their relationship with identified units. Quicker methods of analysis with less accuracy and precision, such as the handheld analyses presented in this study, should be interpreted with added caution. When additional stratigraphic and textural controls are used, methods such as this can be just as valuable as high precision methods. In particular, the speed and cost-effectiveness of this method allow a large number of samples to be analyzed for comprehensive regional composition frameworks. Anomalous samples whose compositions determined by handheld do not agree with their stratigraphic relationships or textural identifications are excluded from the framework based on potential unreliability in the measurements. These samples are then easy targets for analysis by high precision methods.

The proposed chemostratigraphic framework (Fig. 11) agrees with previous observations of chemical variations in the Mendon (Byerly, 1999; Thompson-Stiegler et al., 2010, 2011) but differs in its interpretations. None of the analyzed samples have compositions that appear outside of observed stratigraphic order. However, no stratigraphic section contains a complete representation of all units seen in the Mendon. The cause of these stratigraphic complexities will be discussed in the next section. This complication makes it effectively impossible to describe a

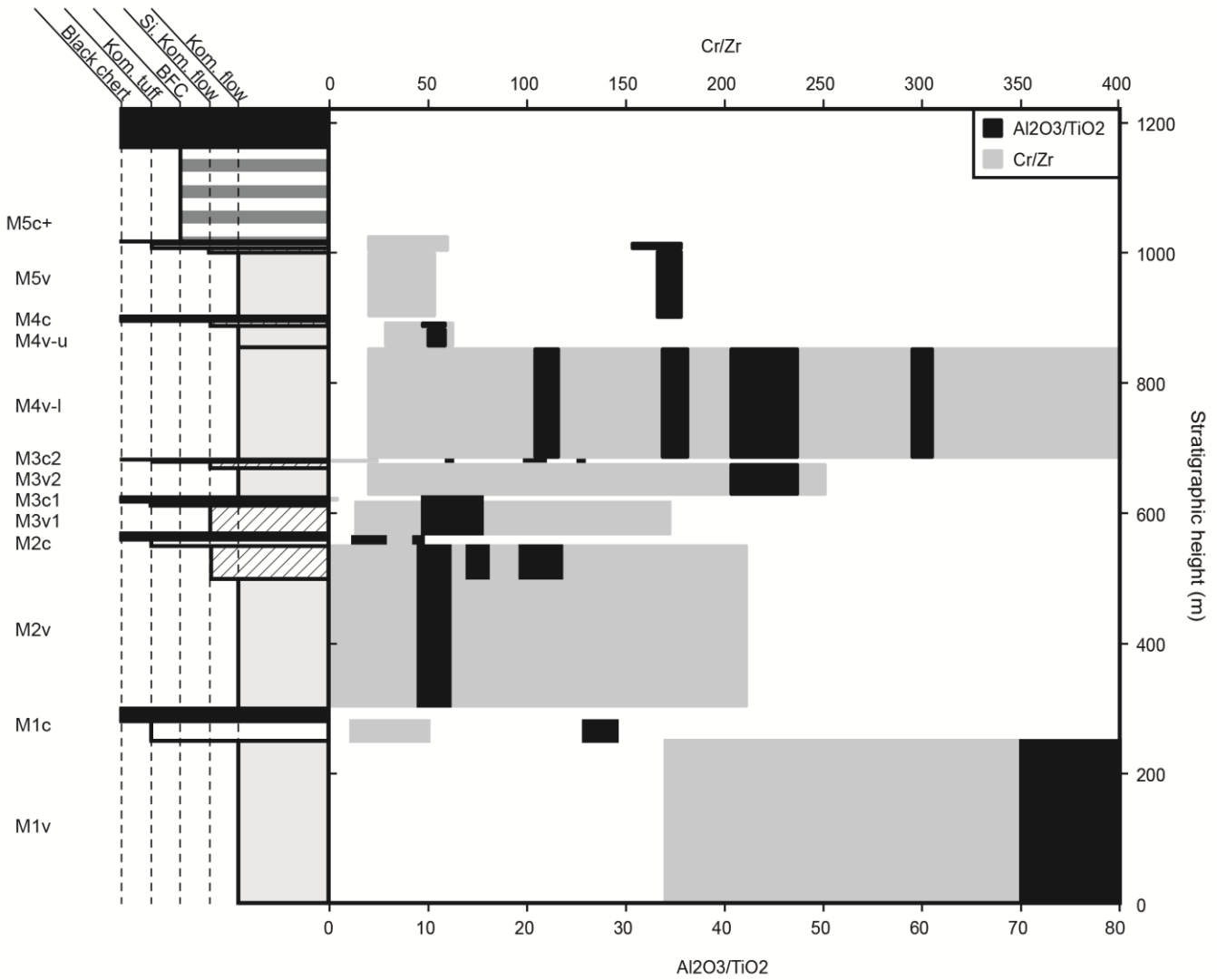

Figure 11. Schematic composite chemostratigraphic section representing all cycles present in the Mendon. Black and grey fields represent typical Al2O3/TiO2 and Cr/Zr ratio ranges respectively. Profile on the stratigraphic section represents both lithology and weathering.

section that is representative of the entire Mendon. Any complete stratigraphic description of the Mendon will necessarily disagree with many local observations (Figs. 6 and 7). In the interest of characterizing all of the events involved in the formation of the Mendon and its entire range of chemical variation, it is still necessary to create a composite stratigraphy comprising type sections of every cycle of the Mendon. The chemostratigraphy proposed here (Fig. 11) represents such a section and assigns a maximum aggregate thickness of at least 1200 m for the Mendon. The ranges of Al_2O_3/TiO_2 ratios provided with this stratigraphy represent the most common ratios for each unit. For compositionally complex units that may represent flows from multiple sources, such as M4, additional Al_2O_3/TiO_2 ratios are also included. Cr/Zr ratios are represented as ranges across all different sources. Considering the number of units of limited extent that have been found, it is likely that there are more flows or tuffs in the Mendon that are not represented by the presented range of compositional variation.

The largest departure from previously proposed stratigraphies is the redefining of M3 and M4. M3 is usually considered as consisting of approximately 50 m of silicified komatiitic flow rock capped by 1 m of chert that may contain a distinctive tuff. This is then followed by up to 400 m of komatiitic flows representing M4v. No tuffs have previously been recognized within M4, and due to the wide range of compositional variation in M4v, Byerly (1999) divided the unit into lower (M4v-l) and upper (M4v-u) portions. Samples in three sections analyzed in this study contain tuffs that are chemically (Fig. 8) and texturally (Fig. 4) similar to M3c within the lower portions of M4. These tuffs typically overlie approximately 50 m of komatiite with Al_2O_3/TiO_2 ratios of 41-47 and Cr/Zr ratios of ~80. This systematic chemostratigraphic variation observed in multiple locations argues for a more detailed classification of this portion of the upper Mendon. This author proposes that the basal portion of M4v-l and the distinctive chert that caps it be

reclassified as M3v2 and M3c2 and that what has been previously classified as M3 be referred to as M3v1 and M3c1. M4v-l would then refer to the thick, layered ultramafic unit where most of the chemical variation in M4 is witnessed. No definitive chemostratigraphy has been created for this unit, because it is believed that its chemical variation may be a result of melt differentiation and fractional crystallization. This reclassification does not greatly influence existing stratigraphies or maps but allows for correlation of M3 everywhere the distinctive tuffs of M3c1 and M3c2 are present.

6.2. Relationship to the Weltevreden Formation

The Weltevreden is confirmed to be age-correlative with the uppermost Mendon and basal Fig Tree based on new Mendon and Fig Tree U/Pb ages (Fig. 10) and the Weltevreden Re/Os date of 3266 ± 8 Ma from Connolly et al. (2011), but there is no apparent genetic relationship between these formations. The range of compositions in the Weltevreden lies within the fields of AUK and AEK (Fig. 9). Flows and tuff units of both compositional types are found interstratified throughout the formation. The wide range of compositions and chemostratigraphic relationships observed in the Mendon Formation have not been seen in the Weltevreden, suggesting that it was far removed from the eruptive source that produced those compositions. The Weltevreden likely represents a period of volcanism in a location affected by one or more sources of magma generated by melting at different depths (Thompson-Stiegler et al., 2012). Meanwhile, the Mendon appears to have had a more complex compositional history that is probably the result of multiple sources.

6.3. Volcanism and Basin Relationships

Subtle changes in stratigraphy from section to nearby section grade into larger differences in further removed sections. Stratigraphy contrasts most notably in sections separated by large faults (Figs. 2 and 3). These observations have led to the suggestion that the Mendon was deposited diachronously across multiple, potentially widespread environments that may even correspond to different basins or sub-basins (Byerly et al., 1996). Sedimentological evidence suggests that stratigraphy from lower-to-upper Mendon cycles represents deposition moving from shallow, possibly shelfal environments to deeper marine settings (Lowe, 1999b). This facies change and diachronous thickening of section has been attributed to syndepositional rifting (Byerly, 1999; Lowe, 1999a; Lowe and Byerly, 2007). This rifting may explain why M1v and the Msauli Chert are virtually absent from more northern sections. However, it is also possible that they are simply not exposed in these sections, as the base of the Mendon is not exposed in them.

Further stratigraphic complexities are observed on a much more local scale. Lowe (1999b) traced flows along strike into banded ferruginous cherts that are interpreted to be their lateral equivalents. This interpretation is supported by the appearance of these cherts in place of flows between capping cherts with distinct tuff layers. These lateral lithologic variations and changes in flow thickness are probable functions of distance from the vent or volcanic field from which the flows erupted (Thompson-Stiegler et al., 2010). A small number of sections, such as the 620 section (Fig. 7), contain some of the most complete records of silicified tuffs available but lack the flows and some of the correlative banded ferruginous cherts that the tuffs typically overlie. One possible explanation is that their presence or absence is also a function of distance from the vent. Another more likely explanation, considering the proximity of these sections to

others that contain the missing flows, the large distances over which these flows were deposited, and the presence of banded ferruginous cherts in the base of some sections like the 620, is that the Mendon is deposited into multiple basins or sub-basins and that some of these basins were isolated from some flows by topographic features that may have been evolving over the course of Mendon deposition. A larger number of sections have been identified that display an opposing situation where some tuff layers are absent. They may contain a record of effusive volcanism but lack tuff layers in their capping, interflow cherts. An example of such a section is Umbaumba Gorge (Fig. 6), where tuff layers are entirely absent from M3c1. M3v1 is a special case in Mendon stratigraphy where the flow rocks and the overlying tuff units are compositionally related. For cases where M3c1 is absent directly above M3v1, the most likely explanation is that the section was deposited upwind of the eruption column. For the much more common case where a flow is typically overlain by a chemically unrelated tuff layer, the section may have either been deposited upwind or located too far away from the vent to receive fallout. Another common occurrence highlighted by this study is the variation of M4 outcrops. It has been noted in previous studies that M4 varies greatly in thickness over its areal extent (Byerly, 1999), and is not known to have produced pyroclastic material (Thompson-Stiegler et al., 2010). Pyroclastic material related to M4v has still yet to be found, and the stratigraphic variation of the flow thickness is further confirmed. The local variation of its thickness may be related to post-depositional structural complexity in the area (Byerly, 1999). Varying amounts of accommodation space could also explain this change in thickness. If the unit was deposited into multiple basins of different dimensions, less accommodation space in smaller basins could result in a thinner section. The lack of related fallout layers could suggest that the vents might not have built up to shallow water depths and thus not end with a phreatomagmatic phase suggested for

lower eruption cycles (Thompson-Stiegler et al., 2011). The absence of pyroclastic layers could also be explained by the basin being upwind from the vent. Whichever is the case, it is probable that there were many vents that terminated in a non-explosive manner and were not preserved in exposed outcrops.

Other sections have been identified with unique cases, such as the 620 section (Fig. 7), where tuff layers compositionally related to M5v are found instead of M5v itself. The abundance of such local and regional variations suggests that the Mendon-type volcanism spanned such an initially large area that it affected multiple basins and was formed by multiple synchronous volcanic fields with compositionally distinct melts. The frequency and degree of these local and regional variations further supports the hypothesis that ascription of a single representative section for even most Mendon outcrops is not possible. Many of these variations over short distances are possibly the result of later tectonic juxtaposition of Mendon basins into the configuration we see today.

6.4. Tectonism

There has been much controversy over whether subduction-related tectonics operated in the Archean. One of the more contentious aspects of Archean tectonics is the timing of the onset of these modern styles (Armstrong et al., 1990; de Wit, 1998; de Wit et al., 2011; de Wit et al., 1987; Furnes et al., 2013; Furnes et al., 2011; Grove and Parman, 2004; Hamilton, 1998; Kröner and Layer, 1992; Lowe and Byerly, 2007; Parman et al., 2004; Shirey and Richardson, 2011; Smithies et al., 2009; Smithies et al., 2007; Van Kranendonk, 2011a, b; Van Kranendonk et al., 2007; Van Kranendonk et al., 2009). Mid-Archean supracrustal sequences like the BGB and the Pilbara have become important subjects in this debate, because they are some of the oldest, best

preserved rocks on the planet and represent a window into the processes of crustal formation and recycling on the early Earth.

The results presented in this study provide evidence for a model of BGB formation dominated by magmatic accretion (Byerly, 1999; Byerly et al., 1996; Lowe, 1999b; Lowe and Byerly, 2007; Van Kranendonk et al., 2009) throughout the Onverwacht and evidence for intermittent felsic volcanism. The Mendon is almost exclusively composed of komatiitic flow rocks interbedded with cherts. Komatiitic pyroclastic tuffs account for the bulk of these cherts. Thompson-Stiegler et al. (2011) estimates komatiitic pyroclasts make up >95% of the interflow sediments in M1c, 30-75% of M2c, and ~65% of M3c. M4c and M5c are exceptions, as they contain little to no pyroclastic material. Orthochemical and biogenic sediments dominate the remaining thickness of chert. There is a near complete absence of epiclastic material in these interflow units, suggesting that there was little to no input from large crustal blocks or arc-related environments. These thicknesses of simatic crust with very little felsic or epiclastic material are in agreement with the formation of the Mendon Formation as an oceanic plateau (Lowe, 1999a; Van Kranendonk, 2011a) generated by plume-related komatiitic volcanism (Arndt, 2003; Arndt et al., 1997; Byerly, 1999; Thompson-Stiegler et al., 2010) in the absence of modern styles of subduction. A small number of felsic tuffs have been identified in the Mendon (Figs. 4 and 8), some of which have been used to constrain its age such as those with zircons analyzed in this study (Fig. 10 and Tables 3a, 3b, and 4) or the tuff in M3c dated by Byerly et al. (1996). The presence of these tuffs in the Mendon indicates there was some type of intermittent felsic volcanism occurring during this time, but their paucity indicates that these were likely not as voluminous and did not play as great a role in crustal formation.

Perhaps the most interesting aspect of Mendon stratigraphy is the sharp transition from effusive and pyroclastic komatiitic volcanism in the Onverwacht to dacitic volcanism and associated volcaniclastics in the Fig Tree marked at its top by the S2 spherule layer. S2 has been interpreted as a quenched liquid silicate droplet fallout layer of impact origin (Lowe and Byerly, 1986; Lowe et al., 1989; Lowe et al., 2003). Two other impact spherule layers have been identified in the lower Fig Tree, one of which typically marks the boundary between the Weltevreden and Fig Tree. It has been suggested that these impacts may have been a controlling or influential factor in the transition from anorogenic to orogenic depositional and deformational styles at the Onverwacht-Fig Tree boundary (Byerly et al., 1996; Lowe et al., 1989; Lowe et al., 2003). Glikson and Vickers (2006) attempted to find correlative impact spherules in the Pilbara. While preserved spherule layers were not found, contemporaneous deformation, mega-clasts, and Fe-rich sediments were correlated to the S2-4 impact layers. The juxtaposition of these lithologies has been compared to mega-clasts and Fe-rich sediments found to be associated with other late-Archean impacts (Glikson, 2008). Recent studies have also suggested that tectonic events from the formation of large igneous provinces, hotspots, rifting, and dike swarms to the onset of plate tectonics itself might have been the result of impact-related mechanisms such as decompression melting (Elkins-Tanton and Hager, 2005; Elkins-Tanton et al., 2004; Glikson, 2001; Jones et al., 2002), lithospheric thinning and fracturing (Hansen, 2007; Ruiz, 2011), and antipodal focusing of impact energy (Boslough et al., 1994; Hagstrum, 2005). The previously suggested possibility that impacts may have been an influential factor in the onset of subduction (Byerly et al., 1996; Glikson, 2008; Glikson and Vickers, 2006; Lowe et al., 1989; Lowe et al., 2003) is supported by the sharp contact in all exposed locations of the Mendon-Fig Tree boundary and confirmation in multiple locations of the incidence of a spherule layer at this

crucial transition (Figs. 6 and 7); however, this evidence is not enough to confirm a correlation between the impacts and the onset of subduction in the BGB. Further constraint on the evolution of similar systems and the feasibility of impact-forcing of tectonics is needed before we can understand the possibility of a causal relationship of this nature in the BGB.

7. Conclusions

A chemostratigraphic framework has been constructed for the Mendon Formation that conforms to previous descriptions of Mendon stratigraphy but also recognizes stratigraphic variations of chemistry within cycles that likely represent multiple synchronous sources. This stratigraphy can be used to place sections into a temporal and stratigraphic context based on their chemical, textural, and spatial relationships. While this stratigraphy holds true for general, regional trends, much local variation has been observed that deviates from the expected stratigraphy. These variations are probably the result of flows being deposited into multiple basins from multiple sources. The original spatial relationships of these basins to the active volcanic fields and their accessibility to flows likely produced these local-scale variations. Such variations make ascription of one representative section to the entire Mendon Formation impossible, but they also provide insight into the depositional environments that existed during Mendon deposition.

This detailed chemical stratigraphy allows for more direct comparison of the Mendon and Weltevreden Formations. While new age data confirms that they are partially age-correlative, geochemical analyses suggest that there is little similarity between the two. Weltevreden samples fall within the ranges of Mendon compositions, but they likely represent different sources within those ranges. These samples lack the extreme compositional variation seen in the Mendon, indicating that they formed separately from the volcanic fields that the Mendon is sourced from. These disparate terranes were subsequently tectonically juxtaposed.

The lithologies recorded in the Mendon Formation and Fig Tree Group indicate that modern styles of tectonics were not active in the BGB during deposition of the Onverwacht Group but began shortly after it ended. The almost exclusively ultramafic nature of this >1 km

thick formation is probably the result of formation by plume-like processes. A small number of felsic ashes indicate that some form of subduction may have been operating, but their paucity, as well as that of epiclastic sediments, suggests that it was not a dominant mechanism. The transition to more modern styles of tectonics occurs abruptly at the Mendon-Fig Tree boundary and is directly incident with at least two major impact layers. These layers and a number of other impact layers found on either side of this transition may have played some role in the onset of subduction in the BGB.

References

Armstrong, R.A., Compston, W., de Wit, M.J., Williams, I.S., 1990. The stratigraphy of the 3.5-3.2 Ga Barberton Greenstone Belt revisited: A single zircon ion microprobe study. Earth and Planetary Science Letters 101, 90-106.

Arndt, N., 2003. Komatiites, kimberlites, and boninites. Journal of Geophysical Research: Solid Earth 108.

Arndt, N.T., Kerr, A.C., Tarney, J., 1997. Dynamic melting in plume heads: the formation of Gorgona komatiites and basalts. Earth and Planetary Science Letters 146, 289-301.

Boslough, M.B., Chael, E.P., Trucano, T.G., Crawford, D.A., Campbell, D.L., 1994. Axial focusing of impact energy in the earth`s interior: A possible link to flood basalts and hotspots.

Byerly, G.R., 1999. Komatiites of the Mendon Formation: Late-stage ultramafic volcanism in the Barberton Greenstone Belt. Geologic Evolution of the Barberton Greenstone Belt, South Africa: Geological Society of America Special Papers 329, 189-211.

Byerly, G.R., Kröner, A., Lowe, D.R., Todt, W., Walsh, M.M., 1996. Prolonged magmatism and time constraints for sediment deposition in the early Archean Barberton greenstone belt: evidence from the Upper Onverwacht and Fig Tree groups. Precambrian Research 78, 125-138.

Byerly, G.R., Lowe, D.R., Wooden, J.L., Xie, X., 2002. An archean impact layer from the Pilbara and Kaapvaal cratons. Science 297, 1325-1327.

Campbell, I.H., Griffiths, R.W., Hill, R.I., 1989. Melting in an Archaean mantle plume: heads it's basalts, tails it's komatiites. Nature 339, 697-699.

Connolly, B.D., Puchtel, I.S., Walker, R.J., Arevalo, R., Piccoli, P.M., Byerly, G., Robin-Popieul, C., Arndt, N., 2011. Highly siderophile element systematics of the 3.3Ga Weltevreden komatiites, South Africa: Implications for early Earth history. Earth and Planetary Science Letters 311, 253-263.

de Wit, M.J., 1998. On Archean granites, greenstones, cratons and tectonics: does the evidence demand a verdict? Precambrian Research 91, 181-226.

de Wit, M.J., Furnes, H., Robins, B., 2011. Geology and tectonostratigraphy of the Onverwacht Suite, Barberton Greenstone Belt, South Africa. Precambrian Research 186, 1-27.

de Wit, M.J., Hart, R.A., Hart, R.J., 1987. The Jamestown Ophiolite Complex, Barberton mountain belt: a section through 3.5 Ga oceanic crust. Journal of African Earth Sciences (1983) 6, 681-730.

Duchac, K.C., Hanor, J.S., 1987. Origin and timing of the metasomatic silicification of an early archean komatiite sequence, barberton mountain land, South Africa. Precambrian Research 37, 125-146.

Echeverria, L.M., 1980. Tertiary or Mesozoic komatiites from Gorgona Island, Colombia: Field relations and geochemistry. Contributions to Mineralogy and Petrology 73, 253-266.

Elkins-Tanton, L.T., Hager, B.H., 2005. Giant meteoroid impacts can cause volcanism. Earth and Planetary Science Letters 239, 219-232.

Elkins-Tanton, L.T., Hager, B.H., Grove, T.L., 2004. Magmatic effects of the lunar late heavy bombardment. Earth and Planetary Science Letters 222, 17-27.

Furnes, H., de Wit, M.J., Robins, B., 2013. A review of new interpretations of the tectonostratigraphy, geochemistry and evolution of the Onverwacht Suite, Barberton Greenstone Belt, South Africa. Gondwana Research 23, 403-428.

Furnes, H., de Wit, M.J., Robins, B., Sandstå, N.R., 2011. Volcanic evolution of the upper Onverwacht Suite, Barberton Greenstone Belt, South Africa. Precambrian Research 186, 28-50.

Glikson, A.Y., 2001. The astronomical connection of terrestrial evolution: crustal effects of post-3.8 Ga mega-impact clusters and evidence for major 3.2±0.1 Ga bombardment of the Earth–Moon system. Journal of Geodynamics 32, 205-229.

Glikson, A.Y., 2008. Field evidence of Eros-scale asteroids and impact-forcing of Precambrian geodynamic episodes, Kaapvaal (South Africa) and Pilbara (Western Australia) Cratons. Earth and Planetary Science Letters 267, 558-570.

Glikson, A.Y., Vickers, J., 2006. The 3.26–3.24 Ga Barberton asteroid impact cluster: Tests of tectonic and magmatic consequences, Pilbara Craton, Western Australia. Earth and Planetary Science Letters 241, 11-20.

Grove, T.L., Parman, S.W., 2004. Thermal evolution of the Earth as recorded by komatiites. Earth and Planetary Science Letters 219, 173-187.

Hagstrum, J.T., 2005. Antipodal hotspots and bipolar catastrophes: Were oceanic large-body impacts the cause? Earth and Planetary Science Letters 236, 13-27.

Hamilton, W.B., 1998. Archean magmatism and deformation were not products of plate tectonics. Precambrian Research 91, 143-179.

Hanor, J.S., Duchac, K.C., 1990. Isovolumetric Silicification of Early Archean Komatiites: Geochemical Mass Balances and Constraints on Origin. The Journal of Geology 98, 863-877.

Hansen, V.L., 2007. Subduction origin on early Earth: A hypothesis. Geology 35, 1059.

Hanski, E., Huhma, H., Rastas, P., Kamenetsky, V.S., 2001. The Palaeoproterozoic Komatiite–Picrite Association of Finnish Lapland. Journal of Petrology 42, 855-876.

Hofmann, A., 2005. The geochemistry of sedimentary rocks from the Fig Tree Group, Barberton greenstone belt: Implications for tectonic, hydrothermal and surface processes during mid-Archaean times. Precambrian Research 143, 23-49.

Hofmann, A., Harris, C., 2008. Silica alteration zones in the Barberton greenstone belt: A window into subseafloor processes 3.5–3.3 Ga ago. Chemical Geology 257, 221-239.

Innov-X, 2010. Delta Family User Manual: Handheld XRF Analyzers. Innov-X Systems, pp. 1-124.

Jahn, B.-m., Gruau, G., Glikson, A.Y., 1982. Komatiites of the Onverwacht Group, S. Africa: REE geochemistry, Sm/Nd age and mantle evolution. Contributions to Mineralogy and Petrology 80, 25-40.

Johnson, D., Hooper, P., Conrey, R., 1999. XRF analysis of rocks and minerals for major and trace elements on a single low dilution Li-tetraborate fused bead. Advances in X-ray Analysis 41, 843-867.

Jones, A.P., Price, G.D., Price, N.J., DeCarli, P.S., Clegg, R.A., 2002. Impact induced melting and the development of large igneous provinces. Earth and Planetary Science Letters 202, 551-561.

Kröner, A., Byerly, G.R., Lowe, D.R., 1991. Chronology of early Archaean granite-greenstone evolution in the Barberton Mountain Land, South Africa, based on precise dating by single zircon evaporation. Earth and Planetary Science Letters 103, 41-54.

Kröner, A., Layer, P.W., 1992. Crust Formation and Plate Motion in the Early Archean. Science 256, 1405-1411.

Kyte, F.T., Shukolyukov, A., Lugmair, G.W., Lowe, D.R., Byerly, G.R., 2003. Early Archean spherule beds: Chromium isotopes confirm origin through multiple impacts of projectiles of carbonaceous chondrite type. Geology 31, 283-286.

Le Bas, M.J., 2000. IUGS Reclassification of the High-Mg and Picritic Volcanic Rocks. Journal of Petrology 41, 1467-1470.

Lowe, D.R., 1999a. Geologic evolution of the Barberton Greenstone Belt and vicinity. Geologic Evolution of the Barberton Greenstone Belt, South Africa: Geological Society of America Special Papers 329, 287-312.

Lowe, D.R., 1999b. Petrology and sedimentology of cherts and related silicified sedimentary rocks in the Swaziland Supergroup. 329, 83-114.

Lowe, D.R., 1999c. Shallow-water sedimentation of accretionary lapilli-bearing strata of the Msauli Chert: Evidence of explosive hydromagmatic komatiitic volcanism. Geologic Evolution of the Barberton Greenstone Belt, South Africa: Geological Society of America Special Papers 329, 213-232.

Lowe, D.R., Byerly, G.R., 1986. Early Archean silicate spherules of probable impact origin, South Africa and Western Australia. Geology 14, 83.

Lowe, D.R., Byerly, G.R., 1999. Stratigraphy of the west-central part of the Barberton Greenstone Belt, South Africa. Geologic Evolution of the Barberton Greenstone Belt, South Africa: Geological Society of America Special Papers 329, 1-36.

Lowe, D.R., Byerly, G.R., 2007. Chapter 5.3 An Overview of the Geology of the Barberton Greenstone Belt and Vicinity: Implications for Early Crustal Development, in: Martin J. van Kranendonk, R.H.S., Vickie, C.B. (Eds.), Developments in Precambrian Geology. Elsevier, pp. 481-526.

Lowe, D.R., Byerly, G.R., Asaro, F., Kyte, F.J., 1989. Geological and geochemical record of 3400-million-year-old terrestrial meteorite impacts. Science 245, 959-962.

Lowe, D.R., Byerly, G.R., Heubeck, C., 1999. Structural divisions and development of the west-central part of the Barberton Greenstone Belt. Geologic Evolution of the Barberton Greenstone Belt, South Africa: Geological Society of America Special Papers 329, 37-82.

Lowe, D.R., Byerly, G.R., Heubeck, C., Geological Society of, A., 2012. Geologic map of the west-central Barberton Greenstone Belt, South Africa. Geological Society of America, Boulder, Colo.

Lowe, D.R., Byerly, G.R., Kyte, F.T., Shukolyukov, A., Asaro, F., Krull, A., 2003. Spherule beds 3.47-3.24 billion years old in the Barberton Greenstone Belt, South Africa: a record of large meteorite impacts and their influence on early crustal and biological evolution. Astrobiology 3, 7-48.

Ludwig, K., 2001. Squid 1.02, A user's manual: Berkeley, California, Berkeley Geochronology Center Special Publication 2, 22 p.

Ludwig, K., 2003. Isoplot/Ex Version 3.00: a geological toolkit for Microsoft Excel. Berkeley Geochronology Center Special Publication, 70pp 4.

Nesbitt, R.W., Jahn, B.-M., Purvis, A.C., 1982. Komatiites: An early precambrian phenomenon. Journal of Volcanology and Geothermal Research 14, 31-45.

Parman, S.W., Grove, T.L., Dann, J.C., De Wit, M.J., 2004. A subduction origin for komatiites and cratonic lithospheric mantle. South African Journal of Geology 107, 107-118.

Premo, W.R., Castiñeiras, P., Wooden, J.L., 2008. SHRIMP-RG U-Pb isotopic systematics of zircon from the Angel Lake orthogneiss, East Humboldt Range, Nevada: Is this really Archean crust. Geosphere 4, 963.

Ransom, B., Byerly, G.R., Lowe, D.R., 1999. Subaqueous to subaerial Archean ultramafic phreatomagmatic volcanism, Kromberg Formation, Barberton Greenstone Belt, South Africa. Geologic Evolution of the Barberton Greenstone Belt, South Africa: Geological Society of America Special Papers 329, 151-166.

Rouchon, V., Orberger, B., 2008. Origin and mechanisms of K–Si-metasomatism of ca. 3.4–3.3Ga volcaniclastic deposits and implications for Archean seawater evolution: Examples from cherts of Kittys Gap (Pilbara craton, Australia) and Msauli (Barberton Greenstone Belt, South Africa). Precambrian Research 165, 169-189.

Ruiz, J., 2011. Giant impacts and the initiation of plate tectonics on terrestrial planets. Planetary and Space Science 59, 749-753.

Schmitz, M.D., Bowring, S.A., Ireland, T.R., 2003. Evaluation of Duluth Complex anorthositic series (AS3) zircon as a U-Pb geochronological standard: new high-precision isotope dilution thermal ionization mass spectrometry results. Geochimica et Cosmochimica Acta 67, 3665-3672.

Shirey, S.B., Richardson, S.H., 2011. Start of the Wilson cycle at 3 Ga shown by diamonds from subcontinental mantle. Science 333, 434-436.

Siever, R., 1992. The silica cycle in the Precambrian. Geochimica et Cosmochimica Acta 56, 3265-3272.

Smithies, R.H., Champion, D.C., Van Kranendonk, M.J., 2009. Formation of Paleoarchean continental crust through infracrustal melting of enriched basalt. Earth and Planetary Science Letters 281, 298-306.

Smithies, R.H., Van Kranendonk, M.J., Champion, D.C., 2007. The Mesoarchean emergence of modern-style subduction. Gondwana Research 11, 50-68.

Sproule, R.A., Lesher, C.M., Ayer, J.A., Thurston, P.C., Herzberg, C.T., 2002. Spatial and temporal variations in the geochemistry of komatiites and komatiitic basalts in the Abitibi greenstone belt. Precambrian Research 115, 153-186.

Thompson-Stiegler, M., Cooper, M., Byerly, G.R., Lowe, D.R., 2012. Geochemistry and petrology of komatiites of the Pioneer Ultramafic Complex of the 3.3Ga Weltevreden Formation, Barberton greenstone belt, South Africa. Precambrian Research 212-213, 1-12.

Thompson-Stiegler, M., Lowe, D.R., Byerly, G.R., 2008. Abundant pyroclastic komatiitic volcanism in the 3.5–3.2 Ga Barberton greenstone belt, South Africa. Geology 36, 779.

Thompson-Stiegler, M., Lowe, D.R., Byerly, G.R., 2010. The Petrogenesis of Volcaniclastic Komatiites in the Barberton Greenstone Belt, South Africa: a Textural and Geochemical Study. Journal of Petrology 51, 947-972.

Thompson-Stiegler, M., Lowe, D.R., Byerly, G.R., 2011. Fragmentation and dispersal of komatiitic pyroclasts in the 3.5-3.2 Ga Onverwacht Group, Barberton greenstone belt, South Africa. Geological Society of America Bulletin 123, 1112-1126.

Van Kranendonk, M.J., 2011a. Cool greenstone drips and the role of partial convective overturn in Barberton greenstone belt evolution. Journal of African Earth Sciences 60, 346-352.

Van Kranendonk, M.J., 2011b. Geochemistry. Onset of plate tectonics. Science 333, 413-414.

Van Kranendonk, M.J., Hugh Smithies, R., Hickman, A.H., Champion, D.C., 2007. Review: secular tectonic evolution of Archean continental crust: interplay between horizontal and vertical processes in the formation of the Pilbara Craton, Australia. Terra Nova 19, 1-38.

Van Kranendonk, M.J., Kröner, A., Hegner, E., Connelly, J., 2009. Age, lithology and structural evolution of the c. 3.53 Ga Theespruit Formation in the Tjakastad area, southwestern Barberton Greenstone Belt, South Africa, with implications for Archaean tectonics. Chemical Geology 261, 115-139.

Appendix: Handheld XRF Test Analyses

This appendix contains test analyses using the Innov-X Systems Delta Mining Premium handheld XRF device (DP6000) and calibrations applied to correct observed systematic errors.

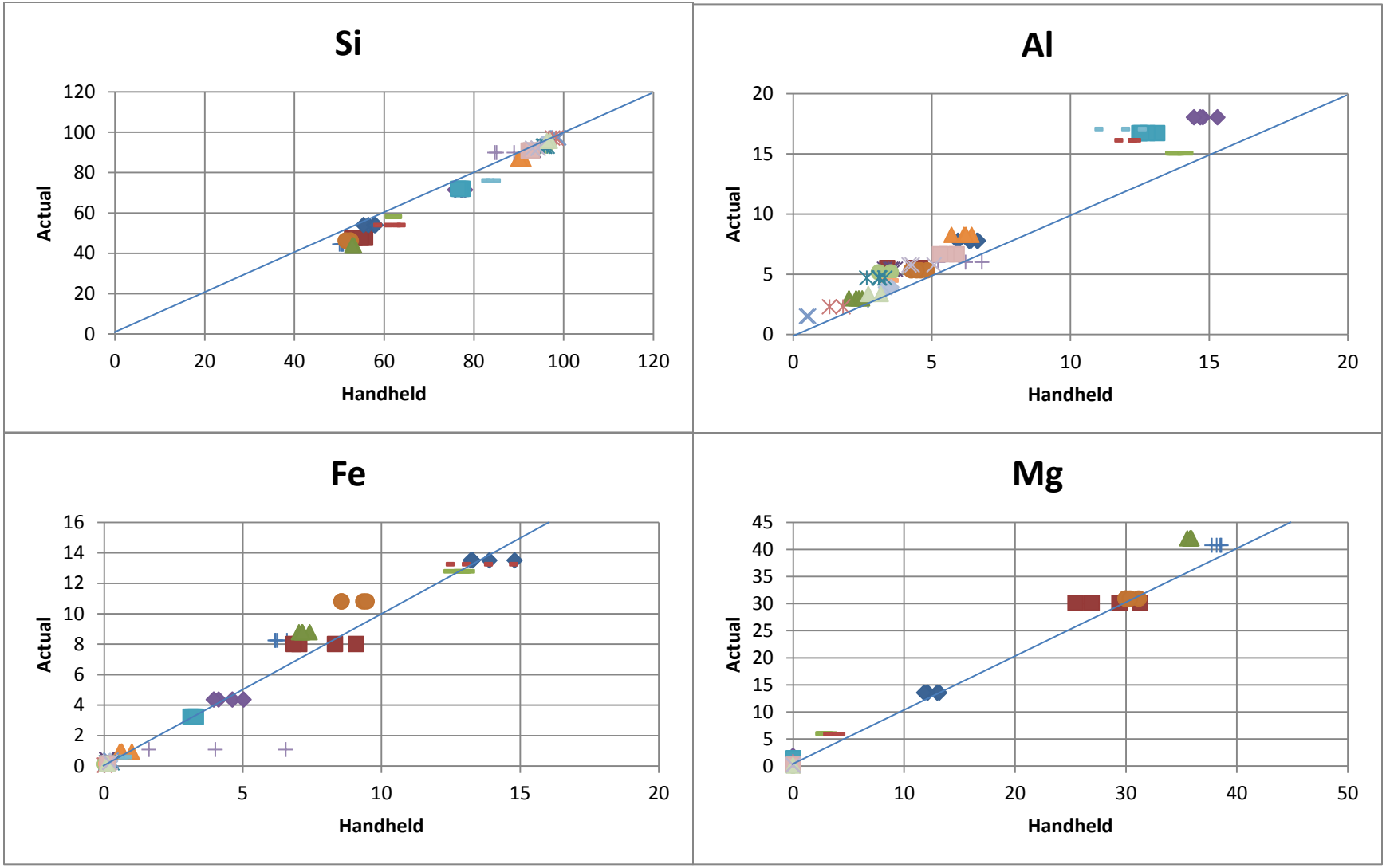

These graphs represent data from initial test runs. Many of these samples and their analyses were not used in calibrations.

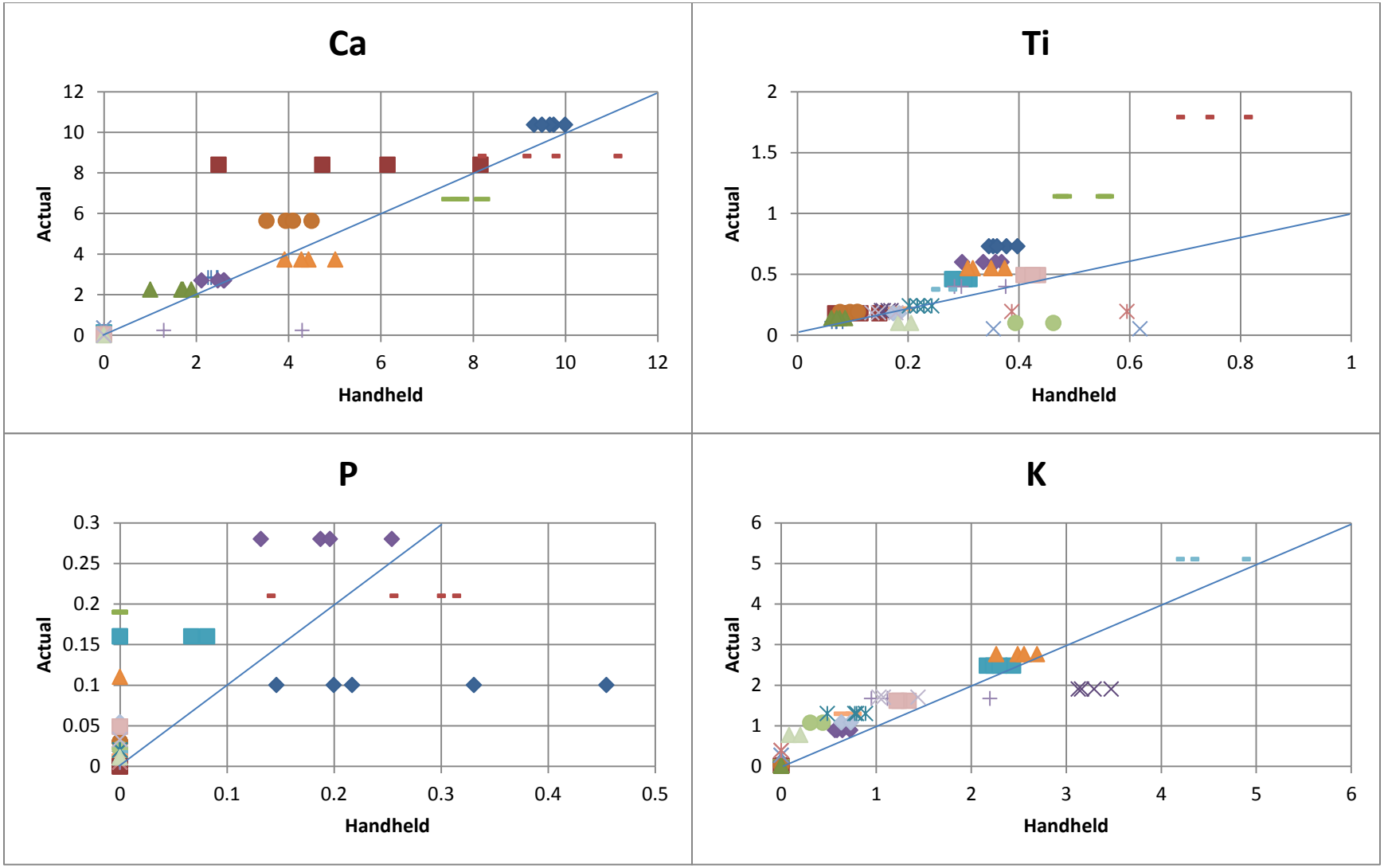

These graphs represent data from initial test runs. Many of these samples and their analyses were not used in calibrations.

Major rock forming element compositions (wt. % oxide) and associated errors reported by the device using Mining+ Mode

Sample	MgO	MgO +/-	Al2O3	Al2O3 +/-	SiO2	SiO2 +/-	P2O5	P2O5 +/-	K2O	K2O +/-	CaO	CaO +/-	TiO2	TiO2 +/-	FeO	FeO +/-	Total	Total*
SA 564-6	29.98	0.98	4.60	0.15	51.46	0.21	0.00	0.07	0.00	0.06	4.50	0.01	0.11	0.01	9.35	0.03	100.00	99.76
SA 564-6	29.97	0.96	4.83	0.15	52.60	0.21	0.00	0.07	0.00	0.06	3.94	0.01	0.10	0.01	8.57	0.03	100.00	98.65
SA 564-6	31.16	0.95	4.26	0.15	52.42	0.21	0.00	0.07	0.00	0.06	3.52	0.01	0.08	0.01	8.55	0.03	100.00	101.14
SA 564-6	30.35	0.95	4.45	0.15	51.52	0.21	0.00	0.07	0.00	0.06	4.10	0.01	0.11	0.01	9.47	0.03	100.00	99.36
KB 12-6	38.61	0.96	2.41	0.13	50.06	0.20	0.00	0.06	0.00	0.05	2.26	0.01	0.07	0.01	6.59	0.02	100.00	103.54
KB 12-6	37.74	0.96	2.70	0.13	50.86	0.21	0.00	0.06	0.00	0.06	2.44	0.01	0.06	0.01	6.19	0.02	100.00	100.69
KB 12-6	38.19	0.95	2.40	0.13	50.70	0.20	0.00	0.06	0.00	0.06	2.47	0.01	0.08	0.01	6.16	0.02	100.00	102.50
KB 12-6	38.51	0.95	2.37	0.13	50.46	0.20	0.00	0.06	0.00	0.06	2.32	0.01	0.07	0.01	6.26	0.02	100.00	102.68
SA 216-9	2.77	0.62	12.11	0.19	61.95	0.21	0.30	0.02	0.00	0.05	9.72	0.02	0.81	0.02	12.35	0.04	100.00	99.41
SA 216-9	2.90	0.60	12.11	0.19	62.97	0.20	0.25	0.02	0.00	0.05	8.11	0.02	0.74	0.02	12.92	0.04	100.00	101.91
SA 216-9	3.97	0.65	12.26	0.19	60.13	0.21	0.14	0.02	0.00	0.05	9.09	0.02	0.69	0.02	13.73	0.04	100.00	99.74
SA 216-9	3.60	0.70	11.61	0.20	57.77	0.22	0.31	0.02	0.00	0.05	11.06	0.02	1.02	0.02	14.63	0.04	100.00	95.34
SA 10-10	2.78	0.62	13.82	0.20	62.08	0.22	0.00	0.07	0.00	0.06	7.68	0.02	0.55	0.02	13.09	0.04	100.00	96.12
SA 10-10	2.74	0.67	13.71	0.20	61.99	0.22	0.00	0.08	0.00	0.07	8.20	0.02	0.48	0.02	12.88	0.04	100.00	93.70
SA 10-10	2.89	0.62	13.76	0.20	62.18	0.22	0.00	0.07	0.00	0.06	7.74	0.02	0.48	0.02	12.95	0.04	100.00	95.73
SA 10-10	3.21	0.61	14.15	0.19	62.07	0.21	0.00	0.07	0.00	0.06	7.49	0.02	0.56	0.02	12.53	0.04	100.00	97.12
SA 44-1	0.00	2.25	14.77	0.18	77.22	0.22	0.25	0.02	0.64	0.01	2.11	0.01	0.37	0.02	4.63	0.02	100.00	93.75
SA 44-1	0.00	2.35	14.68	0.18	77.47	0.22	0.19	0.02	0.59	0.01	2.61	0.01	0.34	0.01	4.13	0.02	100.00	92.40
SA 44-1	0.00	2.30	15.31	0.21	75.85	0.23	0.13	0.02	0.73	0.01	2.60	0.01	0.36	0.02	5.03	0.02	100.00	92.10
SA 44-1	0.00	2.22	14.46	0.18	78.06	0.22	0.20	0.02	0.57	0.01	2.47	0.01	0.30	0.01	3.96	0.02	100.00	93.98
SA 81-2	0.00	1.91	12.49	0.18	77.49	0.22	0.00	0.06	2.17	0.01	4.43	0.02	0.31	0.01	3.11	0.02	100.00	96.40
SA 81-2	0.00	2.00	13.13	0.18	77.26	0.22	0.00	0.06	2.23	0.01	3.91	0.02	0.28	0.01	3.18	0.02	100.00	95.98
SA 81-2	0.00	2.02	12.77	0.18	76.90	0.22	0.07	0.02	2.44	0.01	4.28	0.02	0.30	0.01	3.24	0.02	100.00	94.99
SA 81-2	0.00	1.93	12.55	0.18	76.47	0.22	0.08	0.02	2.30	0.01	5.01	0.02	0.28	0.01	3.31	0.02	100.00	94.37
SA 614-3	0.00	1.41	5.71	0.13	91.07	0.22	0.00	0.05	2.27	0.01	0.00	0.06	0.32	0.01	0.64	0.01	100.00	103.23
SA 614-3	0.00	1.56	6.44	0.13	89.95	0.22	0.00	0.05	2.69	0.02	0.00	0.06	0.35	0.01	0.57	0.01	100.00	103.04
SA 614-3	0.00	1.62	6.16	0.13	89.97	0.22	0.00	0.05	2.49	0.01	0.00	0.06	0.37	0.02	1.00	0.01	100.00	101.49
SA 614-3	0.00	1.60	6.23	0.13	90.28	0.20	0.00	0.05	2.56	0.01	0.00	0.06	0.31	0.01	0.62	0.01	100.00	102.79

*Total before compositions were normalized

Major rock forming element compositions (wt. % oxide) and associated errors reported by the device using Mining+ Mode

Sample	MgO	MgO +/-	Al2O3	Al2O3 +/-	SiO2	SiO2 +/-	P2O5	P2O5 +/-	K2O	K2O +/-	CaO	CaO +/-	TiO2	TiO2 +/-	FeO	FeO +/-	Total	Total*
ND 1-1	0.00	1.36	0.56	0.09	98.56	0.22	0.00	0.04	0.00	0.04	0.00	0.05	0.62	0.02	0.26	0.01	100.00	104.54
ND 1-1	0.00	1.29	0.49	0.09	98.91	0.22	0.00	0.04	0.00	0.04	0.00	0.05	0.35	0.01	0.25	0.01	100.00	105.06
ND 1-4	0.00	1.31	1.32	0.09	98.28	0.20	0.00	0.03	0.00	0.05	0.00	0.04	0.39	0.01	0.02	0.00	100.00	104.71
ND 1-4	0.00	1.22	1.80	0.11	97.57	0.21	0.00	0.03	0.00	0.05	0.00	0.04	0.60	0.02	0.03	0.00	100.00	106.98
ND 1-5	0.00	1.37	3.52	0.11	95.55	0.21	0.00	0.04	0.44	0.01	0.00	0.04	0.46	0.02	0.03	0.00	100.00	106.20
ND 1-5	0.00	1.33	3.09	0.11	96.17	0.21	0.00	0.04	0.31	0.01	0.00	0.04	0.39	0.02	0.04	0.00	100.00	106.32
ND 2-1	0.00	1.91	5.22	0.13	85.07	0.21	0.00	0.05	1.12	0.01	4.30	0.02	0.28	0.01	4.01	0.02	100.00	99.16
ND 2-1	0.00	1.98	6.22	0.13	84.68	0.21	0.00	0.05	0.95	0.01	1.30	0.01	0.30	0.01	6.55	0.03	100.00	100.61
ND 2-1	0.00	1.47	6.81	0.13	89.00	0.22	0.00	0.04	2.20	0.01	0.00	0.06	0.38	0.01	1.62	0.01	100.00	104.63
ND 2-4	0.00	1.60	12.45	0.17	81.82	0.20	0.00	0.04	4.86	0.02	0.00	0.06	0.27	0.01	0.60	0.01	100.00	102.57
ND 2-4	0.00	1.56	10.89	0.15	84.18	0.20	0.00	0.04	4.16	0.02	0.00	0.06	0.24	0.01	0.53	0.01	100.00	103.42
ND 2-4	0.00	1.61	11.86	0.16	82.86	0.20	0.00	0.04	4.32	0.02	0.00	0.06	0.24	0.01	0.72	0.01	100.00	104.06
ND 2-5	0.00	1.35	3.52	0.11	95.44	0.20	0.00	0.04	0.76	0.01	0.00	0.04	0.19	0.01	0.08	0.00	100.00	103.15
ND 2-5	0.00	1.40	3.40	0.11	95.70	0.20	0.00	0.04	0.64	0.01	0.00	0.04	0.18	0.01	0.08	0.00	100.00	102.71
ND 2-6	0.00	1.40	3.35	0.11	95.63	0.20	0.00	0.04	0.63	0.01	0.00	0.04	0.18	0.01	0.21	0.00	100.00	103.33
ND 2-6	0.00	1.31	3.54	0.11	95.34	0.20	0.00	0.04	0.73	0.01	0.00	0.04	0.17	0.01	0.22	0.00	100.00	103.47
ND 4-5	0.00	1.38	5.90	0.13	92.20	0.20	0.00	0.04	1.34	0.01	0.00	0.05	0.43	0.02	0.13	0.00	100.00	104.45
ND 4-5	0.00	1.37	5.54	0.12	92.70	0.20	0.00	0.04	1.24	0.01	0.00	0.05	0.41	0.02	0.11	0.00	100.00	106.51
ND 4-5	0.00	1.35	5.30	0.12	92.94	0.21	0.00	0.04	1.22	0.01	0.00	0.05	0.42	0.02	0.12	0.00	100.00	106.66
ND 4-7	0.00	1.29	2.71	0.11	96.92	0.20	0.00	0.04	0.08	0.01	0.00	0.04	0.18	0.01	0.10	0.00	100.00	103.06
ND 4-7	0.00	1.28	3.16	0.11	96.31	0.20	0.00	0.04	0.20	0.01	0.00	0.04	0.21	0.01	0.13	0.00	100.00	105.27
ND 5-4'A'	0.00	1.38	5.09	0.13	93.07	0.20	0.00	0.04	1.44	0.01	0.00	0.05	0.18	0.01	0.22	0.01	100.00	103.63
ND 5-4'A'	0.00	1.34	4.29	0.11	94.33	0.20	0.00	0.04	1.03	0.01	0.00	0.05	0.13	0.01	0.22	0.00	100.00	104.31
ND 5-4'A'	0.00	1.40	4.19	0.11	94.38	0.20	0.00	0.04	1.07	0.01	0.00	0.05	0.15	0.01	0.21	0.00	100.00	104.22
SA107-2		13.00	0.69	6.35	0.15	56.52	0.21	0.15		0.00	0.05	9.74	0.02	0.35		13.89		110.71
SA107-2		13.18	0.72	5.94	0.16	55.40	0.22	0.33		0.00	0.05	9.99	0.02	0.35		14.81		107.80
SA107-2		12.12	0.69	6.63	0.16	57.88	0.22	0.45		0.00	0.05	9.32	0.02	0.38		13.22		108.59
SA107-2		12.12	0.69	6.41	0.16	57.95	0.22	0.20		0.00	0.05	9.66	0.02	0.36		13.29		107.63
SA107-2		11.82	0.67	6.67	0.15	58.13	0.21	0.22		0.00	0.05	9.49	0.02	0.40		13.28		110.99

*Total before compositions were normalized

Cr, Zr, and Ti compositions (ppm) and associated errors reported by the device using Soil Mode

Sample	Cr	Cr +/-	Zr	Zr +/-	Ti	Ti +/-	TiO2 (wt.% oxide)	TiO2 +/- (wt. % oxide)
ND 1-1	723	11	5.8	1	3384	39	0.565	0.007
ND 1-1	695	11	6.9	1	2123	28	0.354	0.005
ND 1-4	397	8	16.6	1	3435	38	0.573	0.006
ND 1-4	354	8	20.9	1.1	3750	41	0.626	0.007
ND 1-5	91	6	89	2	3224	37	0.538	0.006
ND 1-5	70	6	81.4	1.9	2907	34	0.485	0.006
ND 2-4	2024	21	47.3	1.5	1873	27	0.312	0.005
ND 2-4	1907	20	44	1.4	1567	24	0.261	0.004
ND 2-4	1856	20	41.1	1.4	1709	26	0.285	0.004
ND 4-7	80	4	4.8	0.8	1031	18	0.172	0.003
ND 4-7	84	4	10.6	1	1142	19	0.191	0.003
SA 10-10	33	8	134	4	5666	75	0.945	0.013
SA 10-10	55	8	135	4	5151	71	0.859	0.012
SA 10-10	50	8	132	4	5029	69	0.839	0.012
SA 10-10	35	8	118	3	5749	78	0.959	0.013
SA 81-2	27	4	239	4	2227	33	0.372	0.006
SA 81-2	20	4	199	4	1621	27	0.270	0.005
SA 81-2	35	5	219	4	1923	30	0.321	0.005
SA 81-2	29	4	196	4	1918	30	0.320	0.005
SA 107-2	1430	23	62	2	3548	59	0.592	0.010
SA 107-2	1478	23	62	2	3783	63	0.631	0.011
SA 107-2	1422	23	63	2	3723	62	0.621	0.010
SA 107-2	1397	22	69	2	3759	61	0.627	0.010
SA 107-2	1744	26	70	2	4326	69	0.722	0.012
SA 216-9	99	9	229	5	8807	109	1.469	0.018
SA 216-9	92	9	256	5	8166	101	1.362	0.017
SA 216-9	113	9	223	5	7839	98	1.308	0.016
SA 216-9	124	9	222	5	8224	104	1.372	0.017
SA 564-6	2954	34	8.8	1.1	859	28	0.143	0.005
SA 564-6	2716	31	9.7	1.1	736	26	0.123	0.004
SA 564-6	2950	34	8.9	1.1	919	28	0.153	0.005
SA 564-6	2779	33	11.7	1.1	979	29	0.163	0.005
SA 614-3	1394	16	42.3	1.4	2251	30	0.376	0.005
SA 614-3	1507	17	39.4	1.4	2350	31	0.392	0.005
SA 614-3	1509	17	42.1	1.4	2574	33	0.429	0.006
SA 614-3	1590	17	39	1.4	2316	30	0.386	0.005
SA 902-3	2429	28	6	0.9	425	21	0.071	0.004
SA 902-3	2478	29	5.4	1	526	23	0.088	0.004
SA 902-3	2593	29	5.8	1	477	22	0.080	0.004

Table of measured values, corrected values, and actual values (wt. % oxide) for Al2O3, TiO2, and their ratio

Sample	Al2O3	corr	Actual	Avg	corr Avg	TiO2	corr	Actual	Avg	corr Avg	Al2O3/TiO2	corr	Actual	Avg	corr Avg
ND 2-4	12.45	15.34	17.05	11.73	14.46	0.31	0.38	0.38	0.29	0.35	39.86	39.91	45.28	41.03	41.09
ND 2-4	10.89	13.42	17.05			0.26	0.32	0.38			41.66	41.71	45.28		
ND 2-4	11.86	14.61	17.05			0.29	0.35	0.38			41.59	41.64	45.28		
SA 10-10	13.82	17.03	14.18	13.86	17.07	0.95	1.16	1.07	0.90	1.11	14.62	14.64	13.25	15.43	15.45
SA 10-10	13.71	16.90	14.18			0.86	1.06	1.07			15.96	15.98	13.25		
SA 10-10	13.76	16.95	14.18			0.84	1.03	1.07			16.40	16.42	13.25		
SA 10-10	14.15	17.43	14.18			0.96	1.18	1.07			14.75	14.77	13.25		
SA 81-2	12.49	15.38	16.04	12.74	15.69	0.37	0.46	0.44	0.32	0.39	33.61	33.65	36.45	40.30	40.35
SA 81-2	13.13	16.18	16.04			0.27	0.33	0.44			48.56	48.62	36.45		
SA 81-2	12.77	15.73	16.04			0.32	0.39	0.44			39.81	39.86	36.45		
SA 81-2	12.55	15.47	16.04			0.32	0.39	0.44			39.23	39.28	36.45		
SA107-2	6.35	7.82	7.78	6.40	7.89	0.59	0.73	0.73	0.64	0.79	10.73	10.74	10.71	10.06	10.07
SA107-2	5.94	7.32	7.78			0.63	0.78	0.73			9.42	9.43	10.71		
SA107-2	6.63	8.17	7.78			0.62	0.76	0.73			10.67	10.69	10.71		
SA107-2	6.41	7.90	7.78			0.63	0.77	0.73			10.22	10.23	10.71		
SA107-2	6.67	8.22	7.78			0.72	0.89	0.73			9.25	9.26	10.71		
SA 216-9	12.11	14.92	15.63	12.02	14.81	1.47	1.81	1.73	1.38	1.70	8.24	8.25	9.03	8.74	8.75
SA 216-9	12.11	14.92	15.63			1.36	1.68	1.73			8.89	8.90	9.03		
SA 216-9	12.26	15.10	15.63			1.31	1.61	1.73			9.37	9.38	9.03		
SA 216-9	11.61	14.31	15.63			1.37	1.69	1.73			8.46	8.48	9.03		
SA 564-6	4.60	5.67	5.66	4.53	5.59	0.14	0.18	0.17	0.15	0.18	32.12	32.16	28.60	31.61	31.66
SA 564-6	4.83	5.95	5.66			0.12	0.15	0.17			39.31	39.36	28.60		
SA 564-6	4.26	5.25	5.66			0.15	0.19	0.17			27.78	27.82	28.60		
SA 564-6	4.45	5.48	5.66			0.16	0.20	0.17			27.25	27.28	28.60		
SA 614-3	5.71	7.04	8.26	6.14	7.56	0.38	0.46	0.55	0.40	0.49	15.21	15.23	14.96	15.53	15.55
SA 614-3	6.44	7.93	8.26			0.39	0.48	0.55			16.42	16.44	14.96		
SA 614-3	6.16	7.59	8.26			0.43	0.53	0.55			14.35	14.37	14.96		
SA 614-3	6.23	7.68	8.26			0.39	0.48	0.55			16.13	16.15	14.96		

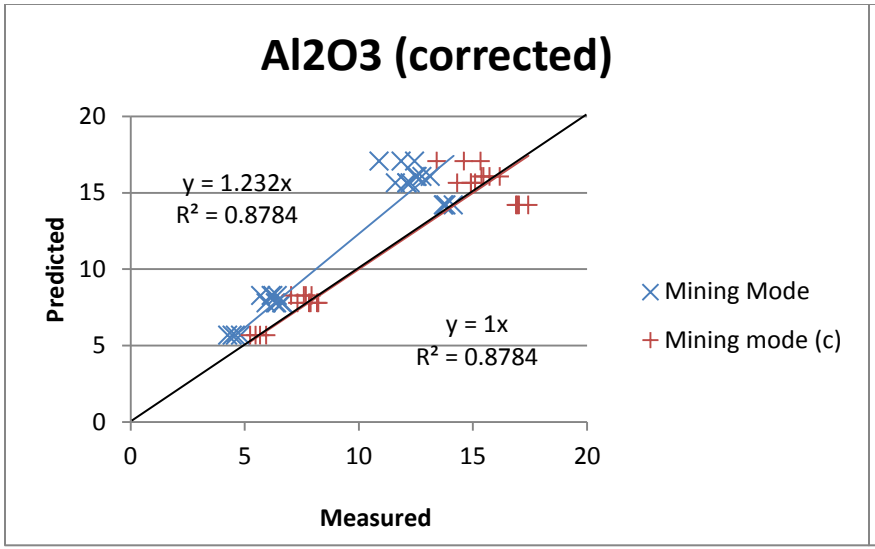
Al2O3 (corrected)
y = 1.232x
R² = 0.8784
y = 1x
R² = 0.8784
Predicted
Measured
Mining Mode
Mining mode (c)

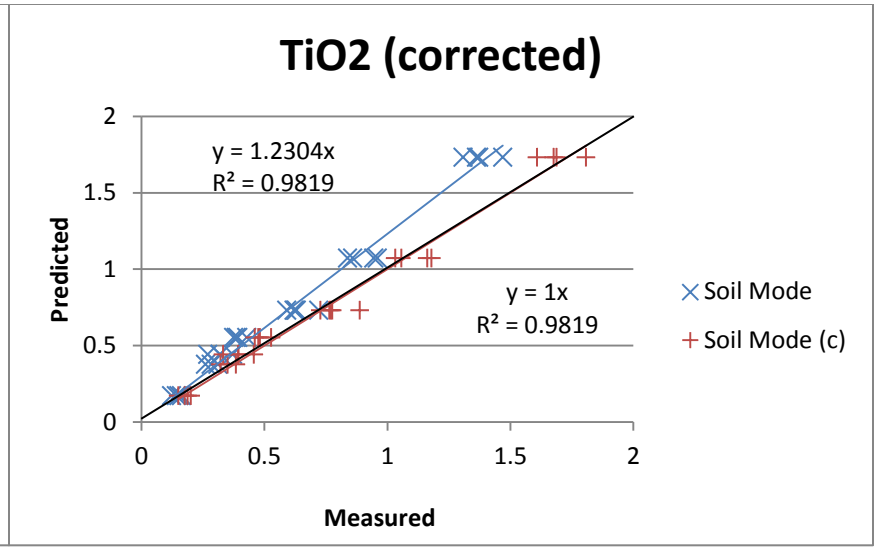
TiO2 (corrected)
y = 1.2304x
R² = 0.9819
y = 1x
R² = 0.9819
Predicted
Measured
Soil Mode
Soil Mode (c)

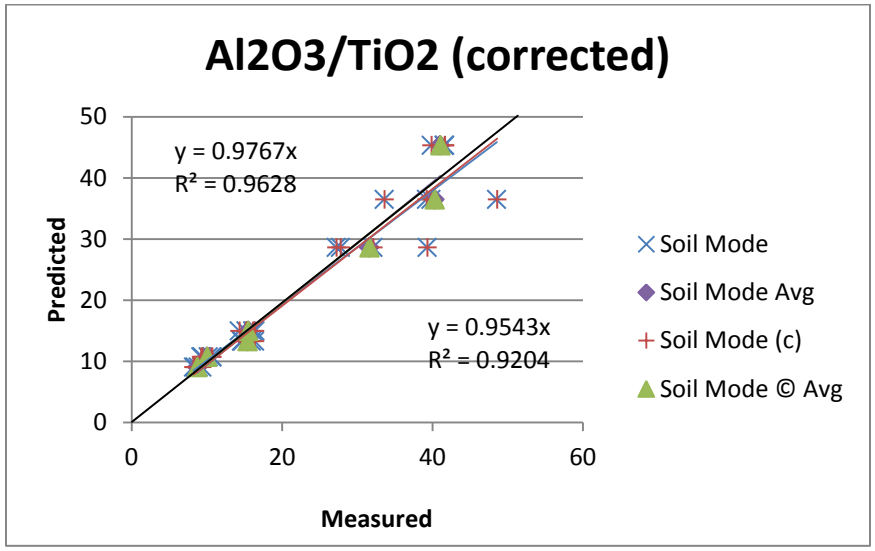
Al2O3/TiO2 (corrected)
y = 0.9767x
R² = 0.9628
y = 0.9543x
R² = 0.9204
Predicted
Measured
Soil Mode
Soil Mode Avg
Soil Mode (c)
Soil Mode © Avg

Table of measured values, corrected values, and actual values (ppm) for Cr, Zr, and their ratio

Sample	Cr	corr	Actual	Avg	corr Avg	Zr	corr	Actual	Avg	corr Avg	Cr/Zr	corr	Actual	Avg	corr Avg
ND 1-1	723	1132.3	877.5	709.0	1110.4	5.8	4.4	3.3	6.4	4.8	124.7	258.7	265.9	112.7	233.8
ND 1-1	695	1088.4	877.5			6.9	5.2	3.3			100.7	209.0	265.9		
ND 1-4	397	621.7	393.2	375.5	588.1	16.6	12.5	11.1	18.8	14.2	23.9	49.6	35.4	20.4	42.4
ND 1-4	354	554.4	393.2			20.9	15.8	11.1			16.9	35.1	35.4		
ND 1-5	91	142.5	21.4	80.5	126.1	89.0	67.2	61.5	85.2	64.3	1.0	2.1	0.3	0.9	2.0
ND 1-5	70	109.6	21.4			81.4	61.4	61.5			0.9	1.8	0.3		
ND 2-4	2024	3169.8	2879.3	1929.0	3021.0	47.3	35.7	34.6	44.1	33.3	42.8	88.8	83.2	43.8	90.8
ND 2-4	1907	2986.6	2879.3			44.0	33.2	34.6			43.3	89.9	83.2		
ND 2-4	1856	2906.7	2879.3			41.1	31.0	34.6			45.2	93.7	83.2		
ND 4-7	80	125.3	97.8	82.0	128.4	4.8	3.6	4.8	7.7	5.8	16.7	34.6	20.4	12.3	25.5
ND 4-7	84	131.6	97.8			10.6	8.0	4.8			7.9	16.4	20.4		
SA 10-10	33	51.7	24.0	43.3	67.7	134.0	101.1	84.0	129.8	97.9	0.2	0.5	0.3	0.3	0.7
SA 10-10	55	86.1	24.0			135.0	101.9	84.0			0.4	0.8	0.3		
SA 10-10	50	78.3	24.0			132.0	99.6	84.0			0.4	0.8	0.3		
SA 10-10	35	54.8	24.0			118.0	89.1	84.0			0.3	0.6	0.3		
SA 81-2	27	42.3	13.0	27.8	43.5	239.0	180.4	153.0	213.3	160.9	0.1	0.2	0.1	0.1	0.3
SA 81-2	20	31.3	13.0			199.0	150.2	153.0			0.1	0.2	0.1		
SA 81-2	35	54.8	13.0			219.0	165.3	153.0			0.2	0.3	0.1		
SA 81-2	29	45.4	13.0			196.0	147.9	153.0			0.1	0.3	0.1		
SA 216-9	99	155.0	116.0	107.0	167.6	229.0	172.8	191.0	232.5	175.5	0.4	0.9	0.6	0.5	1.0
SA 216-9	92	144.1	116.0			256.0	193.2	191.0			0.4	0.7	0.6		
SA 216-9	113	177.0	116.0			223.0	168.3	191.0			0.5	1.1	0.6		
SA 216-9	124	194.2	116.0			222.0	167.5	191.0			0.6	1.2	0.6		
SA 614-3	1394	2183.1	2584.0	1500.0	2349.2	42.3	31.9	41.0	40.7	30.7	33.0	68.4	63.0	37.0	76.7
SA 614-3	1507	2360.1	2584.0			39.4	29.7	41.0			38.2	79.4	63.0		
SA 614-3	1509	2363.2	2584.0			42.1	31.8	41.0			35.8	74.4	63.0		
SA 614-3	1590	2490.1	2584.0			39.0	29.4	41.0			40.8	84.6	63.0		

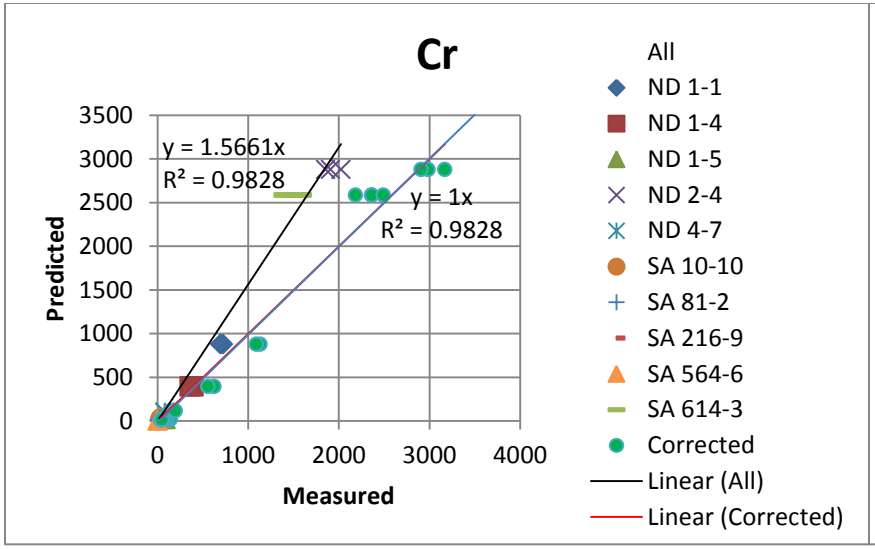
Cr
y = 1.5661x
R² = 0.9828
y = 1x
R² = 0.9828
Predicted
Measured
0
500
1000
1500
2000
2500
3000
3500
0
1000
2000
3000
4000
All
ND 1-1
ND 1-4
ND 1-5
ND 2-4
ND 4-7
SA 10-10
SA 81-2
SA 216-9
SA 564-6
SA 614-3
Corrected
Linear (All)
Linear (Corrected)

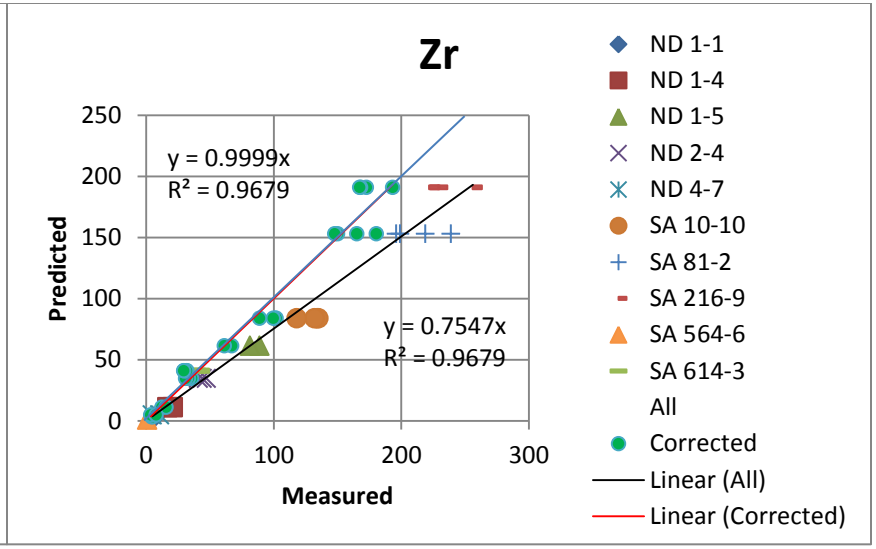
Zr
y = 0.9999x
R² = 0.9679
y = 0.7547x
R² = 0.9679
Predicted
Measured
0
50
100
150
200
250
0
100
200
300
ND 1-1
ND 1-4
ND 1-5
ND 2-4
ND 4-7
SA 10-10
SA 81-2
SA 216-9
SA 564-6
SA 614-3
All
Corrected
Linear (All)
Linear (Corrected)

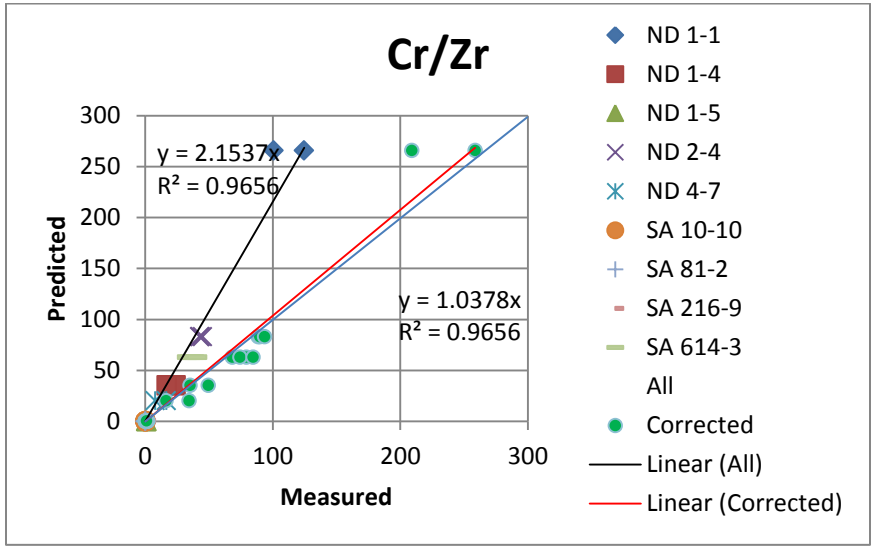
Cr/Zr
y = 2.1537x
R² = 0.9656
y = 1.0378x
R² = 0.9656
Predicted
Measured
0
50
100
150
200
250
300
0
100
200
300
ND 1-1
ND 1-4
ND 1-5
ND 2-4
ND 4-7
SA 10-10
SA 81-2
SA 216-9
SA 614-3
All
Corrected
Linear (All)
Linear (Corrected)

Vita

Nicholas Burns Decker, son of Burns and Susan Decker, was born in Baton Rouge, Louisiana. He graduated from Broadmoor Senior High School in 2006 and enrolled at Louisiana State University to pursue a degree in Computer Science. In the Fall of 2010, he graduated with a Bachelor of Science in Geology. In the Spring of 2011, he began working with Dr. Gary Byerly and, in the Fall of 2011, entered into the Masters program at LSU under him.

During his time at LSU, he spent a field season in South Africa, two summers at the LSU Geology Field Camp in Colorado, and made numerous trips to Big Bend Texas. In his two years as a Masters student, he TAed four different courses: Igneous and Metamorphic Petrology, Mineralogy, Structural Geology, and Summer Field Camp. After he finishes his Masters Program, he will move to Alaska to start in a position with BP.